El Gordo needs *El Anzuelo*: Probing the structure of cluster members with multi-band extended arcs in JWST data

A. Galan[1,2,★], G. B. Caminha[1,2], J. Knollmüller[1,3,4], J. Roth[5,2,6] and S. H. Suyu[1,2]

[1] Technical University of Munich, TUM School of Natural Sciences, Department of Physics, James-Franck-Str 1, 85748 Garching, Germany
[2] Max-Planck-Institut für Astrophysik, Karl-Schwarzschild-Str. 1, 85748 Garching, Germany
[3] ORIGINS Excellence Cluster, Boltzmannstr. 2, 85748 Garching, Germany
[4] Radboud University, Heyendaalseweg 135, 6525 AJ Nijmegen, Netherlands
[5] Technische Universität München (TUM), Boltzmannstr. 3, 85748 Garching, Germany
[6] Ludwig-Maximilians-Universität, Geschwister-Scholl-Platz 1, 80539 Munich, Germany

March 1, 2024

ABSTRACT

Gravitational lensing by galaxy clusters involves hundreds of galaxies over a large redshift range and increases the likelihood of rare phenomena (supernovae, microlensing, dark substructures, etc.). Characterizing the mass and light distributions of foreground and background objects often requires a combination of high-resolution data and advanced modeling techniques. We present the detailed analysis of *El Anzuelo*, a prominent quintuply imaged dusty star forming galaxy ($z_s = 2.29$), mainly lensed by three members of the massive galaxy cluster ACT-CL J0102−4915, also known as *El Gordo* ($z_d = 0.87$). We leverage JWST/NIRCam data containing previously unseen lensing features using a Bayesian, multi-wavelength, differentiable and GPU-accelerated modeling framework that combines HERCULENS (lens modeling) and NIFTY (field model and inference) software packages. For one of the deflectors, we complement lensing constraints with stellar kinematics measured from VLT/MUSE data. In our lens model, we explicitly include the mass distribution of the cluster, locally corrected by a constant shear field. We find that the two main deflectors (L1 and L2) have logarithmic mass density slopes steeper than isothermal, with $\gamma_{L1} = 2.23 \pm 0.05$ and $\gamma_{L2} = 2.21 \pm 0.04$. We argue that such steep density profiles can arise due to tidally truncated mass distributions, which we probe thanks to the cluster lensing boost and the strong asymmetry of the lensing configuration. Moreover, our three-dimensional source model captures most of the surface brightness of the lensed galaxy, revealing a clump of at most 400 parsecs at the source redshift, visible at wavelengths $\lambda_{rest} \gtrsim 0.6\,\mu$m. Finally, we caution on using point-like features within extended arcs to constrain galaxy-scale lens models before securing them with extended arc modeling.

Key words. Galaxies: clusters: general - Galaxies: clusters: individual: ACT-CL J0102−4915 - Galaxies: evolution - Infrared: galaxies - Gravitational lensing: strong - Methods: data analysis

1. Introduction

1.1. Strong gravitational lensing in galaxy clusters

Extending over megaparsec scales and reaching up to quadrillion solar masses, massive galaxy clusters are direct tracers of the cosmic web and its evolution through cosmic time. Galaxy clusters emerge as information-rich targets for jointly studying rare phenomena such as microlensing and caustic-crossing events (e.g., Dai et al. 2020; Williams et al. 2024), distant supernovae (e.g., Rodney et al. 2021; Frye et al. 2024), and probing the cosmological evolution of the Universe (e.g., Abbott et al. 2020; Bocquet et al. 2024). The most massive clusters are made of several hundreds of co-evolving galaxies, showcasing in a single scene the many different stages of galaxy evolution predominantly in the redshift range $z \sim 0 − 1$ (e.g., Wen et al. 2012; Hilton et al. 2021; Klein et al. 2023; Bulbul et al. 2024), probing the transition from a matter-dominated Universe to one driven by dark energy. Additionally, these clusters act as vast permeable screens standing between our telescopes and a plethora of more distant objects, enabling their detection up to redshifts $z \sim 13$ (e.g., Adams et al. 2023; Wang et al. 2023, 2024) and probing

the epoch of reionization. Galaxy clusters do not only magnify these distant objects but also distort and duplicate their images, which can take the form of giant arcs extending over several arcseconds (Bayliss et al. 2011; Cava et al. 2018; Welch et al. 2022). This striking phenomenon, called strong gravitational lensing, is a direct consequence of the extensive gravitational potential of foreground galaxy clusters and their alignment with populations of background sources. A notable property of strong gravitational lensing in clusters is the extreme time delays between the multiple images of time-varying sources, which are used to geometrically measure absolute distances and cosmological parameters (e.g., Caminha et al. 2022; Kelly et al. 2023; Grillo et al. 2024), for which gains in precision are expected specifically with galaxy clusters (Acebron et al. 2023; Bergamini et al. 2024).

Strong gravitational lensing in galaxy clusters is a natural and direct tool to characterize both visible and invisible massive structures of galaxies and their surroundings, which is key to deepen our understanding of their formation and evolution. The high multiplicity of lensed background sources can be used to constrain physical quantities describing individual galaxy members as well as their host dark matter halo through a process

---

★ Corresponding author (aymeric.galan@gmail.com).

called lens modeling. On larger scales, typically out to the virial radius, strong lensing observations can effectively be combined with weak lensing features on the outskirts of clusters (e.g., Bradač et al. 2006; Newman et al. 2013; Umetsu et al. 2018), X-ray and Sunyaev-Zeldovich (SZ) emissions from hot ionized gas in the intra-cluster medium (e.g., Newman et al. 2011; Planck Collaboration et al. 2016). However, at the scale of individual cluster members, challenges arise due to the large angular separation between the lensed images. These images often take the form of unresolved compact clumps within background sources that do not appear in the direct vicinity of cluster members. Such observational constraints necessitate specific modeling assumptions, such as parameterized mass profiles, to ensure that resulting lens models are both tractable and physically plausible (as it is done in e.g., LENSTOOL, Jullo & Kneib 2009). Scaling relations, either based on observed luminosities or stellar kinematics, are also employed to intriduce priors or reduce the number of model parameters (e.g., Bergamini et al. 2019; Caminha et al. 2023). These models are generally sufficient to reproduce the observed lensing features and provide constraints on the fraction of the cluster mass that reside in individual galaxies, as well as measurements of the enclosed mass and dark matter fraction within these galaxies. With more lensing observables, such as extended arcs formed by resolved lensed sources, one can reasonably expect improvements in constraining the internal structure of cluster members, such as their density profiles over kiloparsec scales, and offsets between their baryonic and dark matter components (Schuldt et al. 2019; Wang et al. 2022). As large-volume cosmological simulations improve in resolution—thus simulating more physical processes at smaller scales (e.g., Schaye et al. 2015; Tremmel et al. 2017)—, it is key to constrain higher-order structural properties of cluster members to validate or invalidate predictions from different galaxy formation scenarios.

1.2. The galaxy cluster El Gordo and the galaxy-scale strong lens El Anzuelo

Significant improvements in lens models are achievable for a subset of cluster galaxies that coincidentally appear close in projection to extended lensed images of background sources, often visible as thick gravitational arcs. Alternatively, individual cluster members that are massive enough can create on their own additional strongly distorted and magnified extended arcs (so-called galaxy-galaxy strong lensing events in cluters, e.g., Meneghetti et al. 2023). These arcs are typically much fainter than the foreground lensing galaxies due to their larger distance, smaller intrinsic brightness and redshifted colors. Therefore, high signal-to-noise (S/N) and high resolution observations at wavelengths in which the lensed sources are brighter are necessary to provide useful constraints. In this regard, the James Webb Space Telescope (JWST) and its imaging capabilities in near-infrared wavelengths, have provided the clearest observations of massive galaxy clusters with resolved extended sources. One striking example is the famous merging galaxy cluster CT-CL J0102−4915 at redshift $z = 0.87$, which has been one of the first clusters to be observed with JWST. Since its SZ-based discovery reported in Marriage et al. (2011), several independent analyses confirmed its total mass of $\gtrsim 10^{15}\ M_\odot$ giving it the nickname *El Gordo* as it is the most massive cluster at redshift $z \gtrsim 0.8$, when the Universe was approximately 6 Gyr old (Menanteau et al. 2012; Diego et al. 2023). Recent images acquired using the Near Infrared Camera (NIRCam) on JWST as part of the Prime Extragalactic Areas for Reionization and Lensing Science (PEARLS) Guaranteed Time Observing (GTO) program (Windhorst et al. 2023) have been publicly released in July 2023.

The current state of mass measurements of *El Gordo* (using the SZ effect, weak lensing shape measurements, or strong lensing) is given in Table 1 of Diego et al. (2023). The first strong lensing analysis of the cluster have been achieved by Zitrin et al. (2013) with a light-traces-mass (LTM) model constrained by 9 families of multiple images deduced from Hubble Space Telescope (HST) imaging data. Taking advantage of deeper HST images and thus more image families, Diego et al. (2020) relaxed most of the modeling assumptions from previous works by performing a free-form model of the cluster, obtaining an independent mass measurement. More recently, Caminha et al. (2023) leveraged deep spectroscopic data obtained on the Very Large Telescope (VLT) with the Multi Unit Spectroscopic Explorer (MUSE) to measure the redshifts of 23 multiply lensed galaxies and 167 cluster members, significantly refining the lens model compared to previous works. In our analysis, we make use of both their cluster-scale model their VLT/MUSE data. Two subsequent modeling analysis of *El Gordo* have then been conducted using the JWST dataset from the PEARLS program. Diego et al. (2023) provided 28 new multiply imaged systems and obtained geometric redshifts (i.e., based on an initial lens model) for 37 systems, and then used the full set of 60 families to obtain a new free-form mass model. Shortly after, Frye et al. (2023) performed a new LTM model constrained by 56 multiply image systems to give further evidence of the two-component, cometary-like structure of the cluster, supporting that *El Gordo* is undergoing a major merger event.

The JWST/NIRCam images of *El Gordo* revealed previously unseen features in lensed gravitational arcs, including two remarkable ones that have been recently studied in more details. One is the giant arc *La Flaca* that extends over 20 arseconds, making it one of the longest known gravitational arcs to date. Although already visible in previous HST images, JWST images contain numerous new multiply imaged clumps within the arc, providing constraints on intervening low-mass perturbers in the mass range $10^9 - 10^{10}\ M_\odot$ (Diego et al. 2023). Another remarkable lensing feature of *El Gordo* is called *El Anzuelo*, that we show in the top left panel of Fig. 1. *El Anzuelo* is a multiply imaged galaxy with a redshift of $z = 2.29$ (based on CO line detection at millimeters wavelengths, Kamieneski et al. 2023) that appears as a highly distorted arc, bent around two cluster member galaxies (L1 and L2) and slightly influenced by a third one (L3). Previous HST images of *El Anzuelo*, covering mainly optical wavelengths, feature only one clear distorted image of the background source as shown in the top right panel of Fig. 1. The better sensitivity and resolution of JWST/NIRCam images in the near-infrared reveal that the source is, in fact, multiply imaged at least two times (we find that it is multiply imaged five times). The lensed source, also known as DSFG J010249−491507, is a dusty star forming galaxy whose multiple images have also been detected at radio wavelengths using the Atacama Large Millimeter/submillimeter Array (ALMA, see Cheng et al. 2023). In a recent work, Kamieneski et al. (2023) analyzed in detail the morphology and photometric properties of *El Anzuelo* using a combination of HST, JWST and ALMA datasets, and constructed a simple lens model based on compact multiply imaged features within the arcs. The authors measured the effective size of the lensed galaxy, characterized its dust distribution, and found that star formation is sensibly suppressed in its inner regions, supporting the hypothesis of ongoing inside-out quenching. We extensively compare our modeling results to the the analysis of Kamieneski et al. (2023).
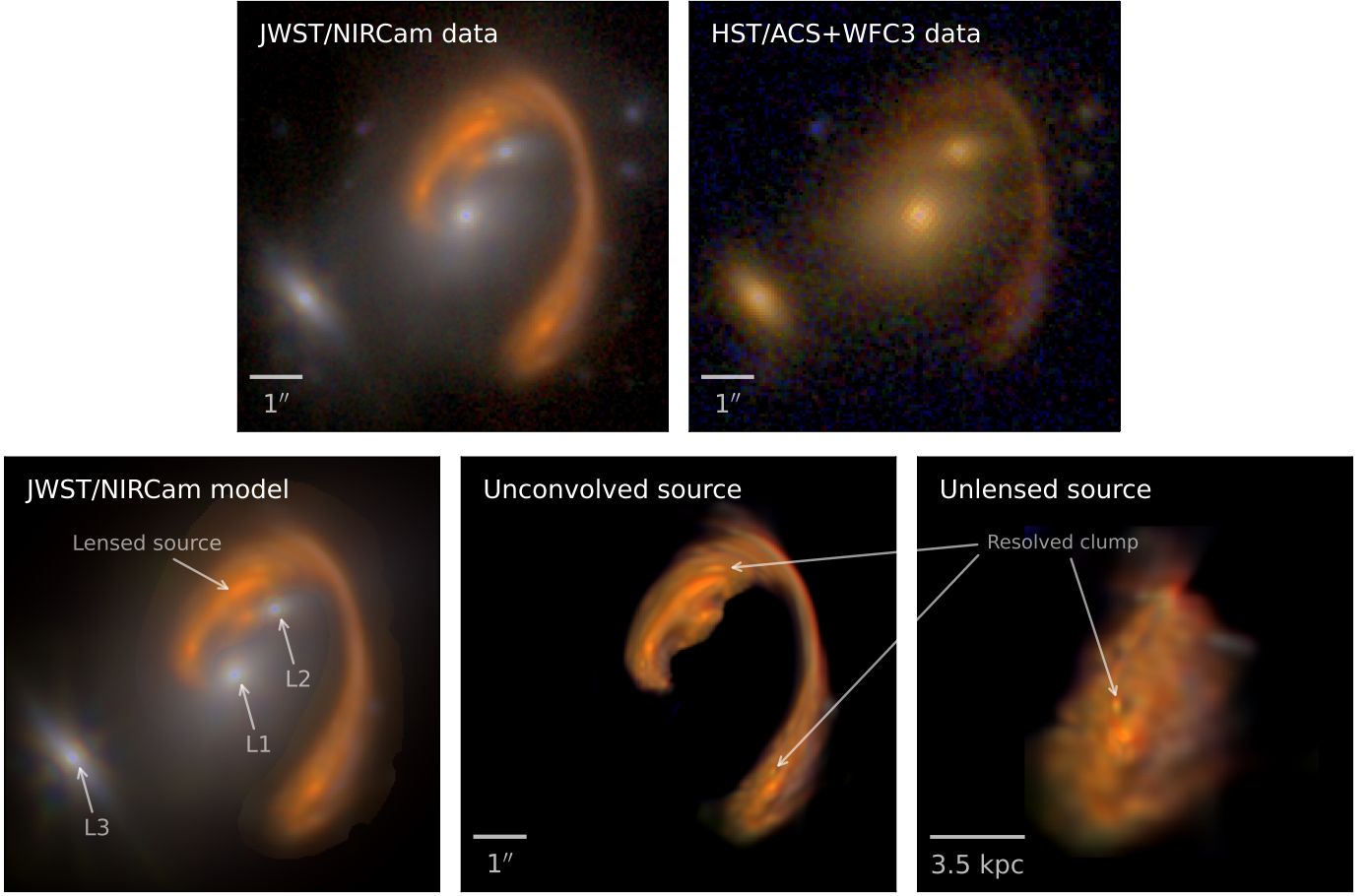
Fig. 1. Color composite images of the dusty star forming galaxy *El Anzuelo* ($z_s \approx 2.3$), strongly lensed by three members of the massive cluster *El Gordo* (L1, L2, L3, $z_d \approx 0.9$). *Top row, from left to right*: color composite built from JWST/NIRCam data used in this work (red: F444W; green: F410M, F356W; blue: F277W, F200W, F150W), archival HST/ACS+WFC3 data shown for comparison (red: F160W; green: F140W, F125W, F105W; blue: F775W, F625W, F606W, F435W). *Bottom row, from left to right*: best-fit model to the JWST/NIRCam data, unconvolved lensed source, unlensed source with arrows indicating the position of a clump revealed in our multi-band model.

1.3. This work: lens modeling of El Anzuelo using a 3D correlated field

The main goal of our work is to conduct the first detailed analysis of the mass distribution of *El Gordo* members using *El Anzuelo* strong lensing features. To this end we should employ a model that is able to capture the complexity of the lensed galaxy over multiple wavelengths, in order to provide stronger constraints on the lens model. We propose to use Gaussian processes, which have been employed in various applications (both within and outside astrophysics) as a mathematically simple yet very versatile model to capture complex correlations observed in data, for an arbitrary number of dimensions. The specific implementation of Gaussian processes we consider here is developed in the Bayesian framework of Information Field Theory (IFT, Enßlin 2019) and is sometimes referred to as *correlated fields*. Some recent astrophysical applications of such fields include the 4D (spatial, time and frequency) reconstruction of the M87 supermassive black hole (Arras et al. 2022), the 3D map of line-of-sight galactic magnetic field in the Milky Way (Hutschenreuter et al. 2023), or the 3D map of the dust distribution in the solar neighborhood (Edenhofer et al. 2023). These recent works have demonstrated that Gaussian processes within IFT can be used to model complex correlations seen in various types of observational data (spatial, temporal, frequency). These results, as well as the efficiency of the accompanying algorithms (low computa-

tion times despite high model flexibility), motivate us to apply a similar strategy to model the highly detailed surface brightness of the lensed dusty star forming galaxy *El Anzuelo*.

In our work we perform pixel-level and multi-wavelength modeling of the extended arcs of *El Anzuelo* as observed in the JWST/NIRCam dataset released by the PEARLS program. Building upon the work of Galan et al. (2022) that introduced the differentiable lens modeling code HERCULENS to describe complex mass and light distributions, we expand the code and use a 3D non-parametric correlated field model implemented in NIFTY (Selig et al. 2013; Steininger et al. 2019; Arras et al. 2019) to model the spatial and spectral morphology of *El Anzuelo* source galaxy. Prior to lens modeling, we use the software package STARRED (Michalewicz et al. 2023) to reconstruct the complex point spread function (PSF) of the instrument. Our modeling pipeline is Bayesian, differentiable and runs on GPU, which significantly improves the computation time necessary to model the many data pixels. We also complement our lensing constraints using stellar kinematics measured on recent MUSE/VLT spectroscopic data using the template fitting software package PPXF (Cappellari & Emsellem 2004; Cappellari 2017). To facilitate the access to our results and encourage future extensions of our analysis, we publicly release our models following the COOLEST lensing standard (Galan et al. 2023).

Two recent works employed lensed source models based on Gaussian processes. Karchev et al. (2022) used layers of Gaussian radial basis functions with predefined correlation lenghts (some of these layers being defined in image plane) to capture the multi-scale nature of highly complex simulated lensed sources. Very recently, Rüstig et al. (2024) validated the lensing application of Gaussian processes and correlated fields within the IFT framework by modeling both simulated and real JWST/NIRCam observations of the strong lens system SPT0418 − 47. Unlike in our work, Rüstig et al. (2024) used a Matérn covariance kernel (in the Fourier domain) for their Gaussian process source model, reserving the use of the non-parametric correlated field to capture complexity in the lens mass distribution.

This paper is organized as follows. In Section 2 we describe the imaging and spectroscopic datasets used in this work. In Section 3, we present stellar kinematics measurements of a subset of the deflectors of *El Anzuelo*, used as a prior in the lens modeling analysis described in Section 4. The resulting models are presented in Section 5, from which we select a subset of key results that are discussed further in Section 6. Finally, we summarize and conclude our work in Section 7.

Throughout this work, we assume a ΛCDM cosmology with $H_0 = 70 \ \mathrm{km \, s^{-1} \, Mpc^{-1}}$ and $\Omega_\mathrm{m} = 0.3$. This cosmology leads to angular sizes of approximately 7.7 kpc arcsec^{-1} at redshift $z = 0.87$ and 8.2 kpc arcsec^{-1} at redshift $z = 2.29$.

2. Data sets

2.1. Imaging data

We primarily use imaging data obtained as part of the PEARLS program (ID: 1176, PI: Windhorst), in particular observations of the cluster ACT-CL J0102−4915 (*El Gordo*) that were publicly released in July 2023 (Windhorst et al. 2023). The *El Gordo* cluster has been selected for PEARLS because of its extreme mass ($M \sim 10^{15} \ M_\odot$), its elongation due to a double-peak post-collision morphology, a large number of lensed sources, and low contamination by intra-cluster light. The PEARLS data set for *El Gordo* consists in NIRCam images in 8 filters—F090W, F115W, F150W, F200W, F277W, F356W, F410M, F444W—covering a wavelength range $0.9 \, \mu\mathrm{m} - 4.5 \, \mu\mathrm{m}$. The acquisitions were all taken on July 29, 2022, and the images were calibrated and reduced as described in great detail in Windhorst et al. (2023). In particular, each individual frame was aligned to the Gaia DR3 reference frame (Gaia Collaboration et al. 2023), such that images in each NIRCam filter are sufficiently aligned for our purposes. We use the FITS files with suffix "_20230718" available on the PEARLS website[1], which include the drizzled science exposures ("_drz") and associated weight maps ("_wht"). All drizzled exposures have a pixel size of 0.″03, and North is aligned with the vertical. We do not use the publicly released data products available on the Mikulski Archive for Space Telescopes, as we notice issues with background subtraction and severe residual noise patterns, which were almost entirely corrected for by the PEARLS reduction (e.g., with careful treatment of $1/f$ noise patterns; Windhorst et al. 2023). The full width at half maximum (FWHM) of the point spread function (PSF) of the NIRCam images of *El Gordo* is in the range 0.″067 − 0.″171 (see Table 1 of Windhorst et al. 2023). The first panel of Fig. 1 shows a color composite image using 6 of the filters from the NIRCam data set.

---

[1] PEARLS website: https://sites.google.com/view/jwstpearls.

Although to a lesser extent, we also use archival HST/ACS+WFC3 data of *El Gordo* from the Reionization Lensing Cluster Survey (RELICS, ID 14096, PI: Coe et al. 2019). We use this data mainly as a check to ensure alignment between (1) the cluster-scale model of Caminha et al. (2023) based on HST, and (2) the JWST/NIRCam data set. We used subset of the filters (drizzled to 0.″06 pixel size) in the top right of Fig. 1.

2.2. Spectroscopic data

We complement JWST imaging data with integral field unit spectroscopic data from the MUSE instrument on the VLT. We use data obtained between December 2018 and September 2019 under the ESO program ID 0102.A-0266 (PI: Caminha), which has been reduced and used in Caminha et al. (2023) to measure redshifts of objects within the field of *El Gordo*. The final datacube covers the wavelength range 4700 Å − 9350 Å (with a gap between 5805 Å and 5965 Å due to laser guiding). The full field-of-view covers an area of $\sim$ 3 arcmin^2, although here we only use a small cutout centered on *El Anzuelo*. The FWHM of these MUSE observations falls in the range 0.″55 − 0.″60 (Caminha et al. 2023). The median average of the datacube centered on *El Anzuelo* and spectra for each deflectors are shown in Fig. 2.

3. Stellar kinematics measurements

3.1. Velocity dispersion measurement

We measure the line-of-sight (LOS) central velocity dispersion from the MUSE observations of Caminha et al. (2023). We first extract integrated spectra for the three deflectors within circular apertures as shown on Fig. 2. The aperture radius is set to 0.″6 which approximately corresponds to the MUSE resolution. For comparison, we also show one dimensional spectra corresponding to the brightest part of the arc, as well as a tentative extraction for L2. For the latter we use an aperture twice as small in order to reduce contamination by L1. We note that we only attempt to measure stellar kinematics of L1 and L3, since L2 would require a proper separation from L1, and the arc is too faint.

We use the spectral template fitting software package PPXF (Cappellari & Emsellem 2004; Cappellari 2017) to model L1 and L3 spectra to measure their line-of-sight central velocity dispersion $\sigma_{v,\mathrm{los}}$ and redshift. As the signal-to-noise (S/N) of the spectra are significantly lower below 6000 Å, we consider only wavelength interval 6650 Å−9300 Å for all kinematics measurements. We run PPXF multiple times in order to marginalize over possible systematic effects due to specific modeling assumptions. First, we vary the orders of the additive polynomial that captures large-scale variations in the continuum, from no polynomial up to order 8 polynomials. Second, we repeat the measurements (with all polynomial orders) varying this time the stellar template library. We use the Indo-US library (Valdes et al. 2004), which has a spectral resolution (FWHM) of $\sigma_{\mathrm{temp,indo}} = 0.57$ Å (for a dispersion of 0.4 Å), and the MILES library (Sánchez-Blázquez et al. 2006), which has a spectral resolution (FWHM) of $\sigma_{\mathrm{temp,miles}} = 1.07$ Å (for a dispersion of 0.9 Å). In empty patches in the vicinity of the lens, we fit Gaussian profiles to 7 sky emission lines to estimate the line spread function (LSF) and find $\sigma_{\mathrm{lsf,obs}} = 1.34$ Å (for a dispersion of 1.25 Å). Assuming a redshift of $z = 0.87$, this leads to a rest-frame value of $\sigma_{\mathrm{lsf,rest}} = 0.72$ Å, which we use as the spectral resolution of the MUSE observations. As the Indo-US library has a better resolution as our spectra, we need to convolve the spectral templates
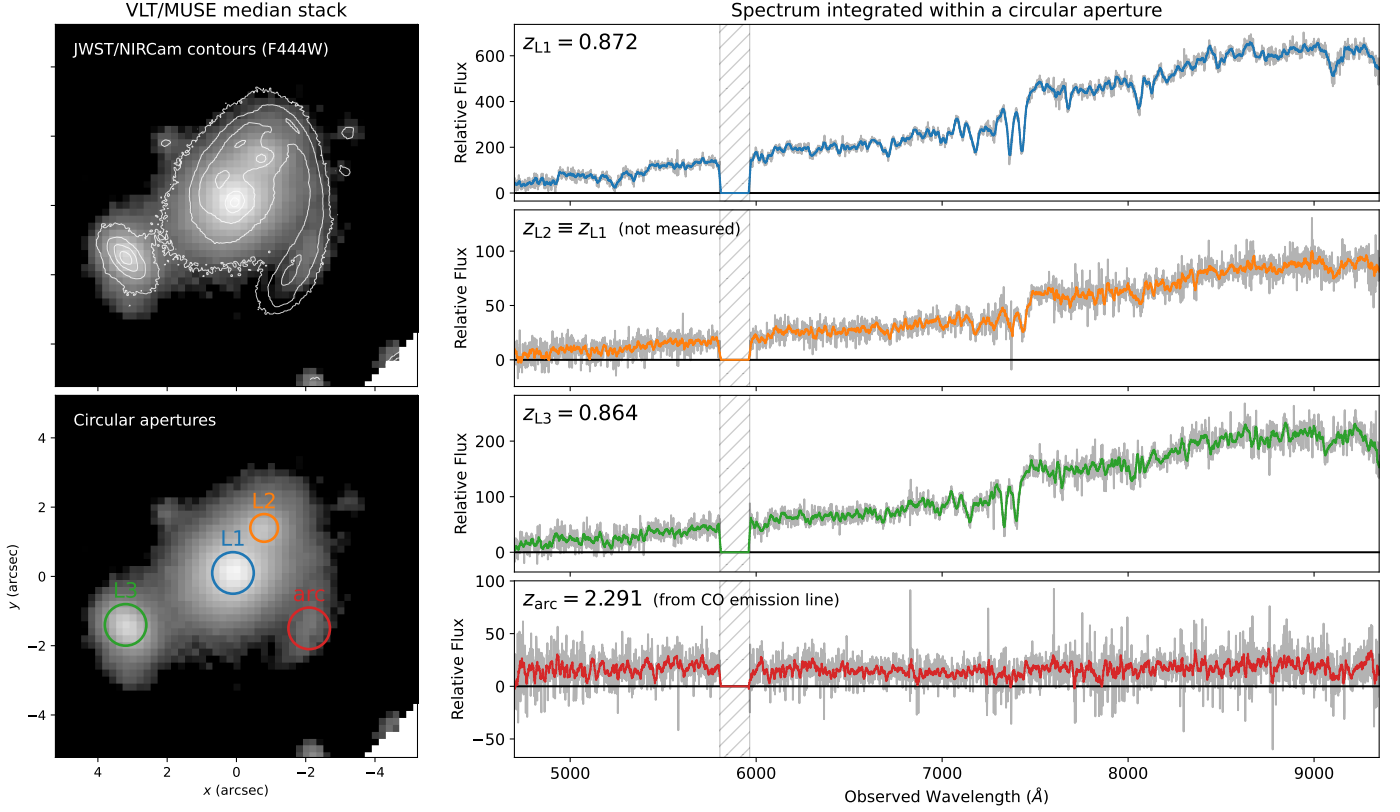
Fig. 2. Extraction of MUSE aperture spectra within circular apertures, for L1, L2, L3 and the western part of *El Anzuelo* arc. Top left panel: luminosity-weighted median stack of the MUSE datacube, with contours from NIRCam/F444W observations. Bottom left panel: MUSE median stack with circular apartures used to extract spectra. Circular apertures have a radius of 0''.6 for L1, L3 and the arc, and 0''.3 for L2. Right panels: corresponding 1D spectra (in gray) in the observed frame, with absorptions lines indicated, as well as smoothed spectra (in color). The estimated redshifts of each component is also indicated; we measure it for L1 and L3, assume that L2 is at the same redshift as L1, and the source redsfhit has been measured in Kamieneski et al. (2023) based on radio observations. The hatched region indicates the gap caused to laser guiding. In this work we only use L1 and L3 spectra to extract stellar kinematics measurements, as L2 is highly blended with L1 and the signal from the arc is too faint.

with a kernel of squared width $\sigma_{\text{diff}}^2 = \sigma_{\text{lsf,rest}}^2 - \sigma_{\text{temp,indo}}^2$ and run the optimization to obtain the best-fit $\sigma_{v,\text{los}}$ value. We apply a similar treatment for measurements obtained with the MILES library; however, these templates have a slightly lower resolution compared to our spectra, thus we apply the correction *after* the PPXF fit in order to retrieve the corrected best-fit $\sigma_{v,\text{los}}$ value (see Eq. 5 of Cappellari 2017). Since PPXF requires an estimation of the noise per wavelength, and the variance from the MUSE data cube is unreliable (see e.g., Sect. 3.1.5 of Bacon et al. 2017), we follow PPXF examples[2] and assume a uniform error equal to unity throughout the entire wavelength range. We emphasize that this choice of noise level does not impact the best-fit values, but only error estimates based directly on the χ^2, which is re-estimated after the fit. To perform all the aforementioned processing steps and measurements, we use an extended version of the PPXF wrapper code VELDIS (Mozumdar et al. 2023).

Fig. 3 shows best-fit spectrum models and stellar velocity dispersion measurements for deflectors L1 and L3. We assume $\sigma_{v,\text{los}}$ to be normally distributed with mean equal to the average among all best-fit values shown in Fig. 3, which is shown as the horizontal line in the right panels. We then consider two error terms for the variance of this normal distribution. The first term σ_{stat}^2 is the variance estimated by PPXF using the diagonal of the parameters covariance matrix at the best-fit position, which cor-

responds to the statistical error. The second term σ_{syst}^2 is the variance among of the best-fit values over all polynomial orders and template libraries, and corresponds to the systematic error. The resulting total $\sigma_{v,\text{los}}$ uncertainty is simply $\sqrt{\sigma_{\text{stat}}^2 + \sigma_{\text{syst}}^2}$, which is indicated as a gray shaded area in the right panels of Fig. 3. The individual error terms σ_{stat} and σ_{syst} are also indicated at the top of these panels. We note that the statistical uncertainty, mainly driven by the S/N of the data, dominates the error budget.

3.2. Contribution from the cluster

We estimate the impact of the cluster scale mass contribution to the kinematics of L1 and L3 in two different ways. The first estimate accounts for the cluster mass within the 0''.6 aperture centered on L1 and L3 (consistently with the measurement aperture), and integrated along the entire line of sight. Hence this estimate is conservative and potentially overestimates the cluster contribution. The second and more realistic method takes into account the three dimensional distribution of the cluster, here assuming it is spherical and using the best fit parameters for the core- and cut-radius obtained in Caminha et al. (2023). We obtain that the additional mass of the cluster component increases the galaxies velocity dispersion by factors of 27% (conservative) or 11% (realistic) for L1, and only 16% or 9% for L3 due to its higher mass (L3 $\gtrsim 1.8 \times$ L1 from Caminha et al. 2023).

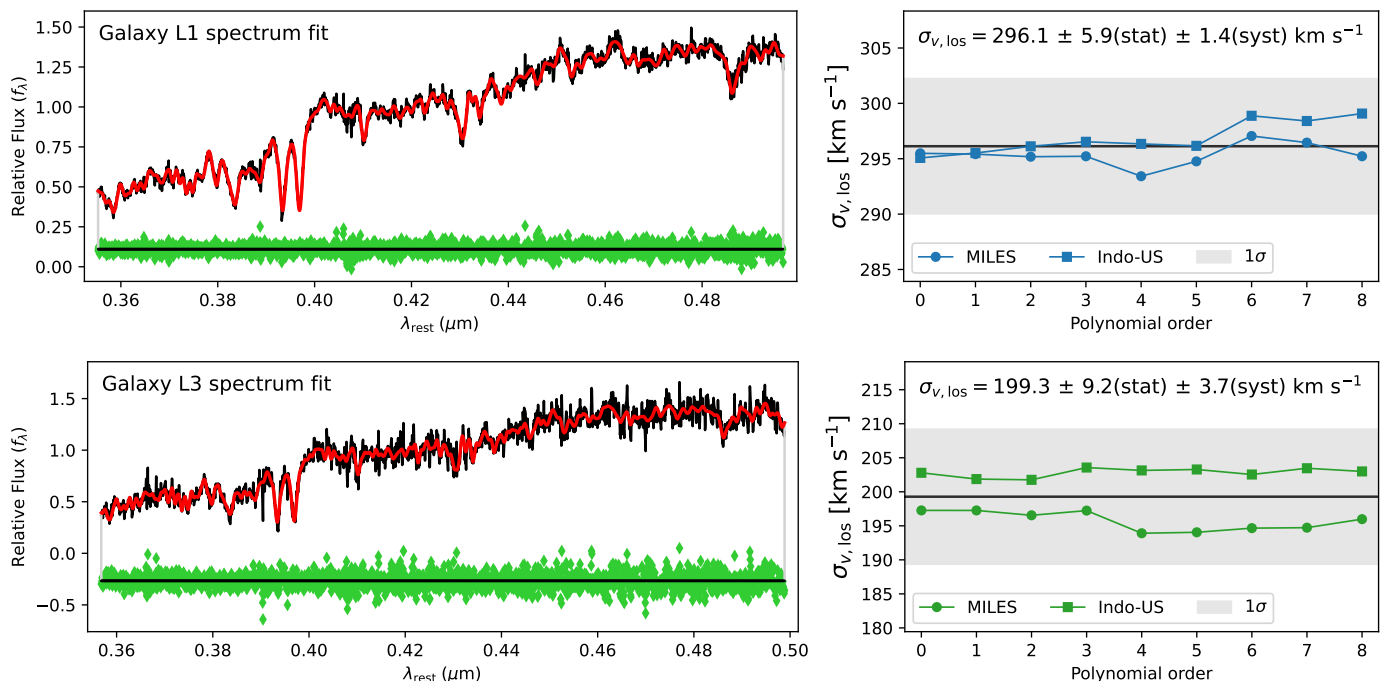[2] https://github.com/micappe/ppxf_examples

Fig. 3. Line-of-sight velocity dispersion $\sigma_{v,\text{los}}$ measurements for deflectors L1 (top row) and L3 (bottom row) from the spectra shown in Fig. 2. *Left panels*: observed spectrum in black, best-fit model in red, and model residuals in green. *Right panels*: best-fit velocity dispersion values for different modeling choices (additive polynomial order and stellar template library). The horizontal black line and the gray shaded area show the mean and 1σ total uncertainty of $\sigma_{v,\text{los}}$, respectively (see Sect. 3 for details). The statistical (stat) and systematic (syst) uncertainties are also separately indicated at the top of the panel.

4. Multi-band lens modeling

4.1. Data pre-processing and exposure map

We convert the data flux units from MJy per steradian to electrons per second using the PHOTMJSR keyword (MJy/sr corresponding to one ADU/s) from the data file header and the instrument gain. We retrieve gain values of 2.05 and 1.85 for the short wavelength (SW) and long wavelength (LW) channels, respectively, from the JWST documentation[3]). We use the weight map obtained from the drizzling step in order to obtain an effective exposure time per pixel. This allows us to correctly take into account the largely different exposure times throughout the field of view, since *El Anzuelo* is located right at the edge of certain dithered exposures (see Sect. 4.5). Since the weight maps provided by the PEARLS team[4] do not contain directly exposure time values, we construct the exposure map as follows. We first retrieve the net exposure time in each filter by dividing the header XPOSURE keyword by the number of detectors of the corresponding NIRCam module (i.e., 8 and 2 for the SW and LW modules, respectively). We then normalize the weight map by dividing it by its maximal value, since we expect the pixel associated to the maximal weight should have the largest exposure time after drizzling. Finally we multiply this normalized weight map by the net exposure time estimated previously, such that the values of the resulting exposure map t_{exp} now ranges from the net exposure time (at maximum) to smaller values for areas with less overlaps between individual exposures. We use this expo-

sure map to estimate the shot noise variance in the data likelihood (see Sect. 4.5).
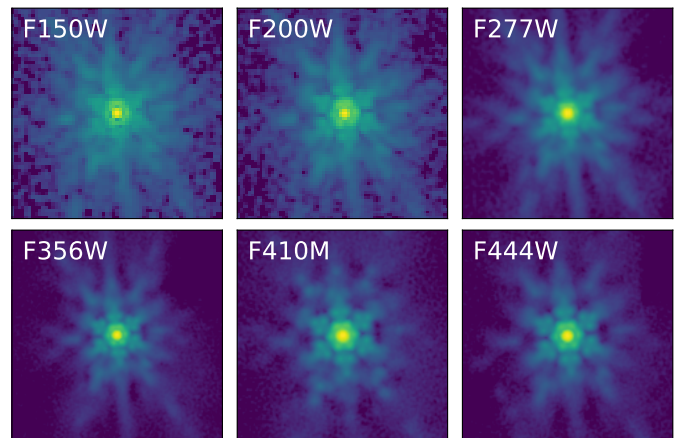

Fig. 4. Point spread function (PSF) models for the main NIRCam filters used in this work, constructed from stars detected in the field. Each cutout has been truncated to 30 times the measured resolution (FWHM) in the corresponding filter. The angular size of the cutouts ranges from approximately 2″ (F150W) to 5″ (F356W).

4.2. Point spread function

Our forward modeling approach incorporates instrumental effects due to the diffraction of light through the telescope by convolving the predicted surface brightness by the point spread function (PSF). We do not rely on a simulated PSF but instead use foreground stars within the field of *El Gordo* to constrain the PSF model, which ensures its consistency

---

[3] https://jwst-docs.stsci.edu/jwst-near-infrared-camera/nircam-instrumentation/nircam-detector-overview/nircam-detector-performance
[4] https://sites.google.com/view/jwstpearls

with the sampling and orientation of the data. We manually select stars that are not saturated, that are bright enough and that do not significantly overlap with nearby objects. We find 4 stars which fulfill these criteria, located at coordinates (01h02m52.02s, −49d14m29.80s), (01h02m49.53s, −49d15m52.62s), (01h02m56.19s, −49d14m32.95s) and (01h02m54.23s, −49d15m02.04s). For band F200W we do not use the last star because it is significantly brighter than the others, such that it can possibly bias the width of the reconstructed PSF. We then extract 201×201 cutouts centered on each star in each filter.

We use the public Python software STARRED[5] (Michalewicz et al. 2023) to construct the PSF model from the selected stars, since Millon et al. (2024) showed that it outperforms other empirical PSF reconstruction methods. We show on Fig. 4 our PSF model in each NIRCam filter. In STARRED, the optimization starts with two dimensional Gaussian profiles that are fitted to each star separately to precisely locate their position within their respective cutout. Then, as an intermediate step, a single Moffat profile, analytically shifted to the positions found in the first step, is jointly fitted to all cutouts simultaneously. The final step consists in optimizing a pixelated grid to fit all PSF features that cannot be captured with analytical profiles. For this step, the Moffat component is held fixed to the best-fit found in the second step. The pixelated background component is regularized with sparsity constraints in wavelet domain. We refer the reader to Michalewicz et al. (2023) and the online documentation for more details about the algorithm. Overall, the resulting PSF model is composed of a Moffat profile superimposed with pixelated deviations that capture local features such as Airy rings and diffraction spikes. STARRED being based on the automatic differentiation library JAX (Bradbury et al. 2018), it can optimize the large number of parameters (of the order of $201^2 \sim 10^4$) using efficient gradient-based algorithms. It takes approximately 3 minutes on a personal laptop to obtain a PSF model in one filter.

4.3. Differentiable multi-band lens modeling

We simultaneously model several JWST/NIRCam bands in which both the main arc and its counter image are visible. As each band in the reduced PEARLS data set is already aligned, we do not add any additional degree of freedom to correct for possible misalignment between the bands. In this work, we explicitly model the mass distribution of L1, L2, and L3 galaxies as main deflectors and take into account the non-uniform mass distribution of the *El Gordo* cluster. The origin $(0'', 0'')$ of our model coordinate system coincides with WCS coordinates $(15.7057851°, −49.2518014°)$ in the JWST/NIRCam data from PEARLS (Windhorst et al. 2023). The pixel size in all bands is $0''.03$, the x axis is positive towards the West, and the y axis is positive towards the North.

As the redshifts of L1 and L3 are slightly different (0.864 and 0.872), we check if these deflectors should be placed on different lens planes. We use the multi-lens plane interface of LENSTRONOMY (Birrer & Amara 2018; Birrer et al. 2021) to estimate the error on the deflection field when assuming a single lens plane at the redshift of L1. More specifically, we compute the maximal deflection angle difference between single-plane and multi-plane deflection fields over the arc region. We find that the deflection angle changes only by $0''.0098$, which is 6.3 times smaller than the JWST resolution in band F150W (FWHM$_{\text{F150W}}$ = $0''.062$ from Table 1 of Windhorst et al. 2023). Therefore, we do not

employ the multi-lens plane formalism in this work, and essentially assume that L1, L2 and L3 are in the same lens plane.

Our baseline model of the deflectors mass distribution is composed of an elliptical power-law (EPL) profile (Tessore & Metcalf 2015) for L1 and L2, and singular isothermal ellipsoid (SIE) profile for L3. Each of these profiles are parametrized by an Einstein radius θ_E, logarithmic (3D) mass density slope γ (an SIE profile has $\gamma = 2$), axis ratio q_m, position angle ϕ_m and centroid (x_m, y_m). In addition, we include in some of our models an external shear field to capture additional angular structures in the mass distribution. The external shear is parametrized by its strength ψ_{ext} and orientation ϕ_{ext}, with origin centered on our coordinate system.

We model the surface brightness of the deflectors using a combination of Sérsic profiles (Sérsic 1963). The Sérsic profile is parametrized by its half-light radius θ_{eff}, Sérsic index n_s, axis ratio q_ℓ, position angle ϕ_ℓ, centroid (x_ℓ, y_ℓ) and amplitude I_{eff} at θ_{eff}. We additionally include a uniform light profile to the lens light model in order to take into account potentially over- or under-subtracted sky level, parametrized by a single intensity I_{bkg}.

For the source surface brightness we use a multi-band pixelated model based on a Gaussian process defined in Fourier space with non-parametric covariance. We refer to Arras et al. (2022) for a complete description of the model, and briefly describe it here for completeness. Our forward source model s can be written as

$$s = \exp\left[F^{-1}(A \odot \xi) + \delta \right], \tag{1}$$

where ξ is a so-called excitation field, A is an amplitude operator, which is the square root of the power spectrum, F^{-1} is the inverse Fourier transform, δ is a uniform offset (in real space) and $\odot$ is the point-wise multiplication. To enforce positivity of the source pixel values, we take the exponential of the Gaussian process. The number of excitation field parameters is $n_\lambda \times n_{\text{src}}^2$, where n_λ is the number of bands and n_{src} is the number of source pixels along each spatial dimensions.

We use the lens modeling code HERCULENS[6] (Galan et al. 2022) that implements the various model components, computes lensing quantities, performs ray-tracing and convolutions with the PSF. For the correlated field model, we use the software package NIFTY[7] (Selig et al. 2013; Steininger et al. 2019; Arras et al. 2019). More specifically, we use the JAX implementation NIFTY.RE (Edenhofer et al. 2024), since HERCULENS is also based on JAX. Our full modeling and inference pipeline is thus differentiable, can be pre-compiled and runs on both CPUs and GPUs.

4.4. Constraints from stellar kinematics

We estimate the Einstein radius of L1 and L3 from their LOS velocity dispersion by assuming a mass distribution following a singular isothermal sphere (SIS) and using the relation

$$\theta_{\text{E,SIS}} = f_{\text{cluster}} \times 4\pi \frac{\sigma_{v,\text{los}}^2}{c^2} \frac{D_{\text{ds}}}{D_s}, \tag{2}$$

where c is the speed of light, D_s and D_s are angular diameter distances to the source and between the deflector and the source, respectively. We add a multiplicative factor f_{cluster} to take into
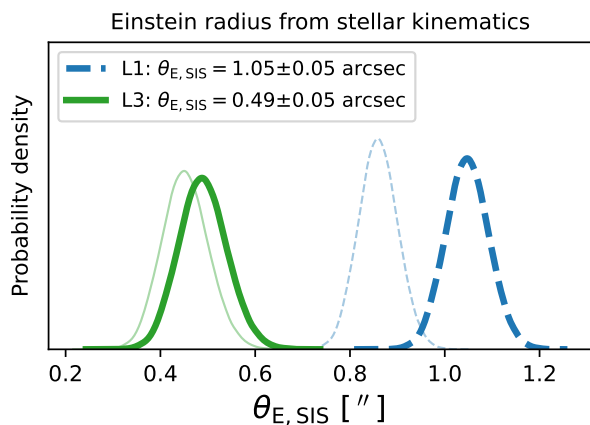
---

[5] https://gitlab.com/cosmograil/starred

[6] https://github.com/Herculens/herculens
[7] https://gitlab.mpcdf.mpg.de/ift/nifty

Fig. 5. Probability distributions for the Einstein radius θ_E of deflectors L1 and L3, based on $\sigma_{v,los}$ measurements shown in Fig. 3, assuming an isothermal (SIS) mass distribution and taking into account the contribution from the host cluster. For comparison, the faint distributions are obtained with the more conservative contribution from the cluster (see Sect. 3.2). For each samples from the $\sigma_{v,los}$ probability distribution, we compute θ_E following Eq. 2. In this work we only use the Einstein radius estimate for L3 to complement lensing constraints, and only show the estimate for L1 for completeness.

Table 1. Dynamical properties of cluster members L1 and L3.

Galaxy	L1	L3
z	0.8722 ± 0.0001	0.8642 ± 0.0002
$\sigma_{v,los}$ [km s^{-1}]	296.1 ± 6.1	199.2 ± 10.0
$\theta_{E,SIS}$ [''], realistic†	$1.05 \pm 0.05^\star$	0.49 ± 0.05
$\theta_{E,SIS}$ [''], conservative†	$0.86 \pm 0.04^\star$	0.45 ± 0.05

Notes. All quantities are inferred from VLT/MUSE data only, and correspond to the redshift z, LOS stellar velocity dispersion $\sigma_{v,los}$ and corresponding Einstein radius $\theta_{E,SIS}$ assuming an SIS mass distribution (Eq. 2). Uncertainties for redshifts and velocity dispersions contain both statistical and systematic uncertainties, adding in quadrature.
$^{(\dagger)}$ The "realistic" and "conservative" cases relate to the estimated contribution of the cluster, described in Sect. 3.2.
$^{(\star)}$ Note that we infer that the density profile L1 is steeper than for an SIS from lensing constraints (Sect. 5.3).

account the cluster contribution to the gravitational potential. As discussed in Sect. 3.2, the cluster realistically contributes to the mass of L1 and L3 at the 11% and 9% levels, respectively, hence we set $f_{cluster,L1} = 1 - 0.11$ and $f_{cluster,L3} = 1 - 0.09$. For angular diameter distances, we compute D_s and D_{ds} corresponding to L1 and L3 using redshift estimates from PPXF fits (i.e., $z_{L1} = 0.872$ and $z_{L3} = 0.864$), and assume $z_s = 2.291$ for the source redshift. The resulting probability distributions lead to $\theta_{E,L1} = 1''05 \pm 0''05$ and $\theta_{E,L3} = 0''49 \pm 0''05$, as shown in Fig. 5 (also compared to the distributions for a more conservative cluster contribution). We summarize in Table 1 the redshift, velocity dispersion and Einstein radius estimates. We emphasize that, to complement lensing constraints, we only use the Einstein radius estimate for L3 consistently with the assumption of an isothermal density profile used in the lens model. As we show in Sect. 4.3, we find that the mass density slope of L1 is steeper than isothermal.
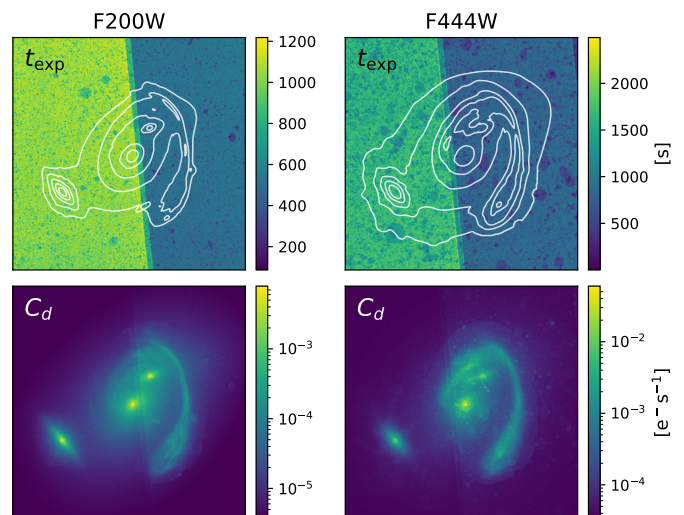
Fig. 6. *Top row*: example exposure maps for filters F200W and F444W. The non-uniform exposure time is due to the combination of dithered exposures and the masking of cosmic rays. White isophotes indicate the position of the arcs and deflectors with respect to features in the exposure map. *Bottom row*: diagonal of the data covariance matrix (i.e., the noise map) estimated from the exposure map and the model-predicted flux to compute the shot noise contribution. The detector edge and cosmic ray imprints are still clearly visible in the noise map and are taken into account during modeling.

4.5. Bayesian framework

We cast the optimization and inference problem in a Bayesian framework to combine the imaging and kinematics datasets. We denote the imaging likelihood $\mathcal{P}(d_{img} | m_{img}(\Theta))$, where d_{img} is the imaging data and m_{img} is the model with parameters Θ. We further assume that data noise follows a normal distribution with diagonal covariance matrix C_d, which results in the following analytical formula for the log-likelihood:

$$\log \mathcal{L}(\Theta) \equiv \log \mathcal{P}(d_{img} | m_{img}(\Theta))$$
$$= -\frac{1}{2}\left[d_{img} - m_{img}(\Theta)\right]^\top C_d^{-1}(\Theta)\left[d_{img} - m_{img}(\Theta)\right]$$
$$+ \log\left(2\pi \sqrt{\det C_d(\Theta)}\right). \quad (3)$$

The first term in Eq. 3 is simply $-\chi^2/2$. The diagonal of the covariance matrix C_d represents the noise variance per data pixel, which is the combination of a constant background noise and the shot noise due to the flux of the object itself. When evaluating Eq. 3, we estimate the shot noise from the model-predicted flux, hence the dependence of C_d on the model parameters Θ. In the case of JWST data of *El Anzuelo*, the data covariance is non trivial because the lens is located at the edge of the detector on some of the individual exposures, as visualized in Fig. 6 on which a diagonal discontinuity is clearly visible after drizzling. We take into account this spatially varying exposure time over the field of view by self-consistently updating C_d during model optimization. Since the data has units of electrons per second, the shot noise variance in C_d corresponding to pixel i is $m_{img,i}/t_{exp,i}$.

We incorporate in the inference the constraints from stellar kinematics data d_{kin} measured in Sect. 4.4 by imposing a Gaussian prior on the Einstein radius of L3:

$$\mathcal{P}(\theta_{E,L3}) \equiv \mathcal{P}(\theta_{E,L3} | d_{kin}) \sim \mathcal{N}(0''49, 0''05) , \quad (4)$$

which corresponds to the distribution shown in Fig. 5.

The probability distribution of the source excitation field follows the standard multi-variate normal distribution. Both source power-spectra (along the spatial and wavelength dimensions) are power-laws in logarithmic scale parametrized by a log-normal prior on the fluctuations amplitude, and a Gaussian prior on the power-law slope. In addition, a global additive offset is added, parametrized by a mean and standard deviation, the latter itself following a log-normal distribution with free mean and width parameters. For the formal Bayesian formulation of the correlated field model, we refer the reader to Arras et al. (2022). Other lens mass parameters are sampled according to either normal or uniform distributions, which we detail in Sect. 4.6.

From a set of different model variations within a given model family, we further follow Bayesian principles and use the Bayesian information criterion (BIC) to weight the different models before marginalization. The BIC is defined as

$$\mathrm{BIC} = n_\mathrm{p} \log(n_\mathrm{d}) - 2 \log \mathcal{L}(\hat{\Theta}) \,, \tag{5}$$

where n_p is the number of optimized model parameters, n_d is the number of data points used to constrain the model and $\hat{\Theta}$ is the set of model parameters that maximize the likelihood function $\mathcal{L}$ defined by Eq. 3. After computing the BIC values associated to each model variation, we can compute the associated (relative) weights based on their BIC difference with the model having the lowest BIC value (i.e., the highest Bayesian evidence). We use the BIC as a proxy for the computationally expensive Bayesian evidence; however, the evidence lower bound (ELBO) used in variational inference can also be used in principle.

At this point, it is important to note that realistically, one can only sparsely sample the space of all possible model variations within a model family. Therefore, we must take into account this sparse sampling and correct the weights by using the scatter in BIC values estimated over the specific set of model variations. We correct the weights using a strategy inspired by recent strong lensing analyses of lensed quasars (e.g., Rusu et al. 2020; Shajib et al. 2020). In particular, we convolve the relative weights based purely on BIC differences by a Gaussian window function whose width is based on the standard deviation of the BIC values (e.g., see Eq. 12 from Rusu et al. 2020). Not correcting for sparse sampling would typically result in only one or two individual models to contribute to the final posterior, which could lead to severe underestimation of parameters uncertainties.

4.6. Modeling sequence

From the original 8 filters of the *El Gordo* data set obtained by PEARLS, we select 6 in which the lensed arcs are clearly visible, namely we discard filters F090W and F115W. These filters also have overall lower S/N with significant non-Gaussian noise patterns. Therefore, we use data in filters F150W, F200W, F277W, F356W, F410M and F444W to constrain our lens models.

We start by modeling the surface brightness of the three deflectors L1, L2 and L3. Based on the NIRCam imaging data these are likely elliptical galaxies, although L2 and L3 have high ellipticities which could be the hint of a disk component. As all three deflectors are very bright and display significant deviations from axisymmetry, several model components a required to model their light distribution to acceptable levels. In particular we use 2 concentric Sérsic profiles for L1 and L2, and 3 concentric Sérsic profiles for L3. We also include a free constant background light component to properly account for any systematic offset from previous background subtraction steps. To maximize the fit quality in each of the six JWST filters and given the limited flexibility of the Sérsic profiles, we optimize lens light parameters in

each bands separately. This single-band fitting step also allows us to measure the scatter in the position of the deflectors light distribution, and further use it as a prior for the centroids of their mass distribution. For each filter, we carefully design a mask to exclude the region containing significant source flux from the likelihood. We also exclude several other luminous objects in the field of view, mostly small galaxies or potential tidal stripping features. The optimization of all parameters is performed using the second-order gradient descent algorithm BFGS (Nocedal & Wright 2006), accessible in HERCULENS as a wrapper for the python package JaxOpt (Blondel et al. 2021). All lens light parameters are then fixed to their best-fit values for subsequent modeling steps.

We first search for an approximate mass model to use as a suitable starting point later on for the full multi-band modeling. The lensing features of *El Anzuelo* being complex, we could not obtain such a mass model by fitting only simple light components such as Sérsic profiles in source plane. Instead, we construct a slightly more elaborate source model by combining a Sérsic profile with a shapelets basis set (Birrer et al. 2017). The shapelets model is implemented in HERCULENS (Galan et al. 2022) as a wrapper around the JAX implementation of GIGALENS (Gu et al. 2022), itself using LENSTRONOMY routines (Birrer & Amara 2018; Birrer et al. 2021). We fix the lens light model and optimize all remaining parameters using the BFGS algorithm.

We then replace this intermediate source model with the 3D correlated field described in Eq. 1. The arc mask is updated such that it encloses all the flux from the source galaxy (importantly, it should also contain areas where its flux decreases to zero). Given a set of mass model parameters, this arc mask dynamically sets the extent of the pixelated grid in the source plane, such that the source grid pixel scale relative to the angular scale of the source remains approximately constant[8]. Beside the arc mask, the overall likelihood mask remains the same as for the lens light fitting step. We converge on a fiducial number of source pixels $n_\mathrm{src} = 100$ along each spatial dimension, by progressively increasing n_src until we observe no significant changes in the residuals (i.e., the reduced χ^2 remains approximately constant). We also find that increasing n_src does not significantly affect the morphology of the lensed galaxy, but only allows to capture more of the compact clumps within its disk, which only cover a negligible fraction of pixels entering the χ^2 calculation. We maintain the lens light parameters fixed to their best-fit values, and jointly fit for the source and lens mass parameters. To allow our model to compensate for imperfect lens light modeling, we add a free uniform amplitude over the arc mask region, independently in each band.

For the mass distribution of L3, we fix all its SIE parameters to their corresponding lens light parameters, except for the Einstein radius as it is the only parameters that can be realistically constrained given its distance to the arcs. For other mass model parameters—center, position angle and axis ratio—we impose broad priors informed by the best-fit values of their lens light model counterpart, although not unreasonably broad to keep the randomly drawn initial parameter values within a physically plausible range. The position angles of the two EPL profiles are sampled from a Gaussian prior with mean centered on the best-fit value from the reference filter (F444W with higher S/N) and a width of 10 degrees. The axis ratio q_m of the EPL profiles are sampled from a uniform prior in the range $[\max(0.5, q_{\ell,\mathrm{ref}} - 3\sigma_q), 1]$, where $q_{\ell,\mathrm{ref}}$ is the axis ratio in the ref-

---

[8] A similar strategy is used in the lens modeling software GLEE (Suyu & Halkola 2010; Suyu et al. 2012).

erence filter and σ_q is the scatter of axis ratio over the filters. This sensible prior on q_m is motivated by previous results that the dark matter, thus the total, mass ellipticity of elliptical galaxies is correlated with their light ellipticity (e.g., Dubinski 1994; Sluse et al. 2012; Shajib et al. 2021, although such correlations may be impacted by selection functon effects). In our case however, our generic choice of axis ratio prior effectively leads to a uniform prior over the interval [0.5, 1] for both L1 and L2. We also allow the center of EPL profiles to vary and assign Gaussian priors with mean and width equal to mean and standard deviation of the positions across the filters of the corresponding light distribution. Thus, all our models allow for a misalignment between the light and total mass distribution of the main deflectors. The logarithmic slopes of the EPL profiles have wide Gaussian priors centered on $\gamma = 2$ with 10% standard deviation, wide enough not to impact the posterior distributions. Finally, for models that include an external shear field, we draw elliptical shear components ($\gamma_{ext,1}$, $\gamma_{ext,2}$) from a Gaussian centered on zero with width 0.05. We check that our inferred results are not prior-dominated by verifying that the aforementioned priors are wider or comparable to the tighter posteriors constrained by the multi-band JWST data.

We use variational inference (VI) to model the joint posterior distribution over the numerous model parameters. More specifically, we use geometric variational inference (GEOVI, Frank et al. 2021), which is able to capture non-linear covariances even in large dimensions. Due to restricted GPU memory, we maintain the number of individual samples used to estimate the Kullback-Leibler divergence (which is the metric optimized in VI) to a relatively low value (we use 32 samples for the last five GEOVI iterations). However, all samples are fully independent and are drawn using antithetic sampling, which leads to a larger effective number of samples and a reduced sampling variance (see Eq. 65 from Knollmüller & Enßlin 2019). We take into account possible systematic errors by performing different optimization runs within a given model family, which we refer to as model variations. We obtain a well-sampled final posterior distribution by approximating the marginalized posterior with a multivariate normal distribution, from which we draw an arbitrary number of samples. The mean and covariance matrix of this normal distribution is computed from the samples of individual model variations, weighted by the relative BIC differences computed as described in Sect. 4.5. We emphasize that while the final joint posterior distribution is, by construction, a linear approximation of the underlying distribution, it is built from GEOVI samples that individually capture the non-linear covariances in the parameter space (Frank et al. 2021).

The lens models considered in this work have $\sim 10^5$ parameters[9] and are constrained by $\sim 10^6$ pixels (excluding pixels outside the masked areas). We note that just-in-time compilation, gradient-based inference algorithms and GPU parallelization all lead to a low computation time. In particular, it takes approximately 140 minutes on a single NVIDIA A100 GPU to obtain one variational inference estimate of the joint posterior distribution, for a given model variation. Increasing the resolution of the source, even significantly, only marginally impacts runtime.

---

[9] The *effective* number of model parameters, in particular due to the field regularization of the source model, is much lower (although it is not explicit).

4.7. Model families

We model the JWST data set assuming three different model families—which can be seen as two intermediary models and one final model—depending on the description of the nearby cluster *El Gordo*. We first consider a "Shear only" model, based on the assumption that *El Gordo*'s deflection field can be approximated by a single external shear component over a field of view of $\sim 10''$ centered on L1. This assumption follows the recent work of Kamieneski et al. (2023), and is also the most common assumption to model nearby massive structures external to the main deflectors.

Instead of a uniform external shear, we build a "Cluster only" model by using one of the most recent lens models of *El Gordo*. We use the model of Caminha et al. (2023) based on HST imaging data and MUSE spectroscopic data (the same data we use in Sect. 3) that allowed the authors to spectroscopically confirm the 23 multiply imaged sources used to constrain the model. This cluster model is parametrized by a set of dual pseudo-isothermal mass density (dPIE) profiles associated to the 243 cluster members and 20 foreground group members, as well as pseudo-isothermal elliptical mass density (PIEMD) profiles associated to each of the two dark matter cluster-scale components of the cluster. For the complete description of the mass model, see Caminha et al. (2023). We note that two other cluster-scale lens models have been recently published by Diego et al. (2023) and Frye et al. (2023), also using the JWST imaging data as in our work. The spectroscopic model of Diego et al. (2023) is based on the same the lensing constraints as Caminha et al. (2023) but follows a non-parametric modeling approach. Such a non-parametric model is expected to be more accurate close to multiple image pairs, but may be less robust further away from these constraints, which is the case at the location of *El Anzuelo* (no constraints from *El Anzuelo* were used in the spectroscopic model of Diego et al. 2023). The model of Frye et al. (2023) is based on the LTM approach, new photo-z measurements and incorporates constraints within the arc of *El Anzuelo*. Since we do not use the mass distribution of L1, L2 and L3 from the cluster-scale model, we expect marginal differences between Caminha et al. (2023) and Frye et al. (2023) models over the field of view of *El Anzuelo*. Therefore, in this work we consider the model of Caminha et al. (2023) after removing the mass components associated to the three deflectors.

The third "Cluster+Shear" model is a combination of the two models above as it contains both an external shear component and the cluster's deflection field. We consider this more advanced model as our fiducial one. The external shear in this case is expected to capture additional azimuthal structures that have not been included in the cluster lens model, such as nearby faint galaxies that are visible in some NIRCam filters. However, as recently recalled by Etherington et al. (2023b), there is no guarantee that external shear captures only structures external to the lens, but can instead compensate for the lack of azimuthal freedom in the main deflectors mass model. In our case, one can also interpret the external shear as a local correction to the cluster deflection field.

5. Results

5.1. Overall fit to the multi-band NIRCam data

Among the model families we consider, the "Cluster+Shear" model provides the best fit to the multi-band imaging data, with a reduced chi-square of $\chi^2_\nu = 1.25$ computed among all fitted data
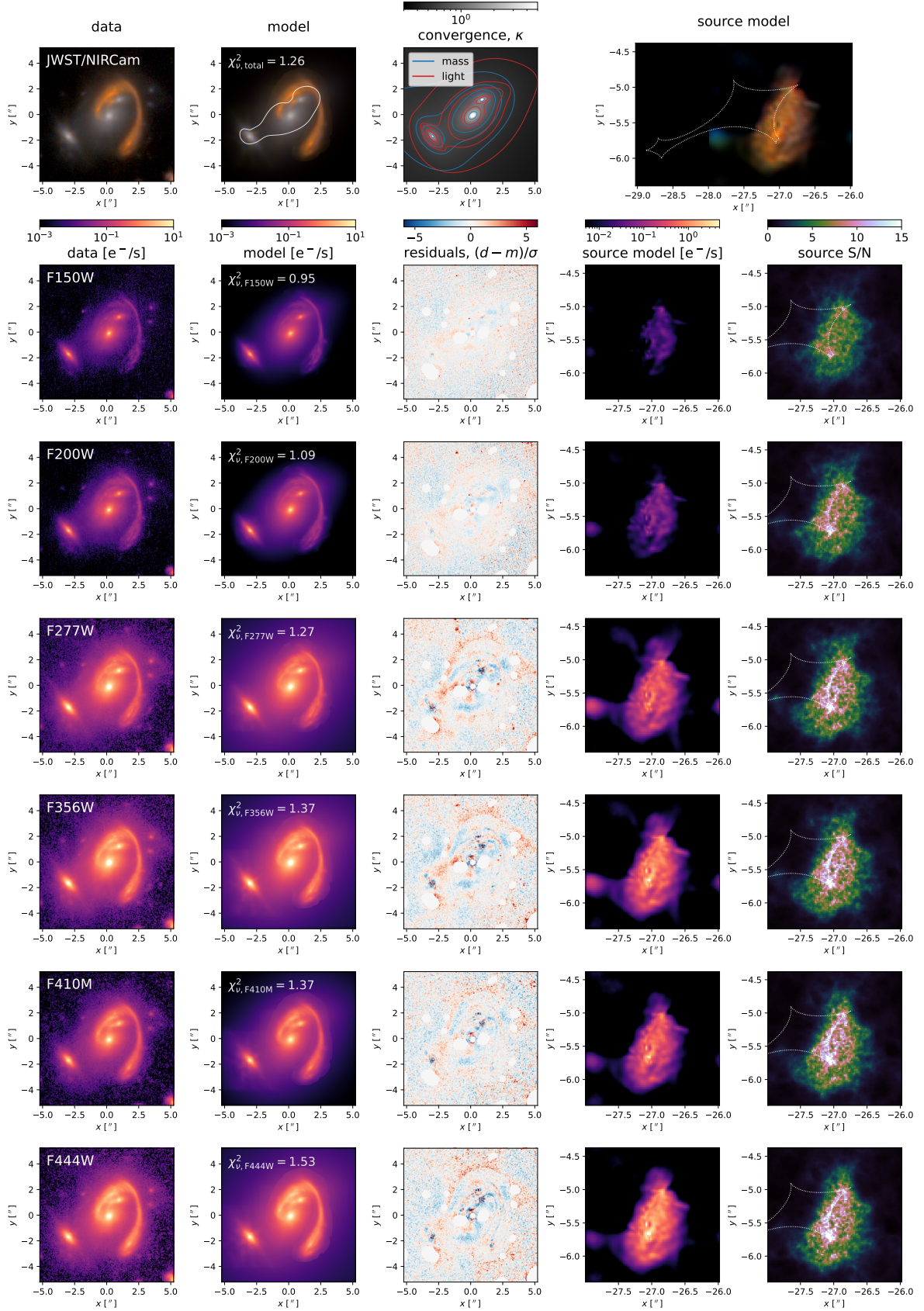
Fig. 7. Mean lens model among the best-fit posterior samples for our fiducial "Cluster+Shear" model. *First row, from left to right*: color image of the data, color image of the model with reduced χ^2 from image residuals (which differs from the full log-likelihood, see Eq. 3), convergence map (with convergence and surface brightness contours), and color image of the unlensed source model. *Remaining rows, from left to right*: data in the indicated filter, model, normalized residuals (areas excluded from the fit appear white), unlensed source model, S/N source map defined as the mean source model divided by the standard deviation of the model posterior in each source pixel. Critical lines and caustics are indicated in some of the panels as white solid line in the image model panel, and dotted lines in the right column panels.

pixels. The "Shear only" model leads to a slightly worse fit with a χ_ν^2 increase of $\gtrsim 0.01$, followed by the "Cluster only" with a further increase of > 0.02. We show in Fig. 7 an instance of the best "Cluster+Shear" model of our baseline setup (i.e., a source model with 100 pixels along each spatial dimensions). As we optimize model parameters using VI, Fig. 7 only shows the model corresponding to the mean among the best-fit VI posterior samples (see caption for the description of each panel). Moreover, we can also use these same samples to divide the mean by the standard deviation of the posterior, which results in a S/N map that we show for the source plane in the rightmost column of Fig. 7.

In the image plane, the model fits remarkably well the data in all bands. The lensed arcs, although containing a large number of features at difference scales, are particularly well fitted. We also note the dynamic range of the source model, which spans more than three orders of magnitudes from fainter structures in filter F150W to the brighter central region in filter F444W. The surface brightness of the L2 and L3 galaxies are also accurately modeled. Small scale residuals that still remain close to L2 and L3 centroids are likely caused by slightly inaccuracies in the PSF model, as they are similar to those of quasar-host separation analyses (e.g., see Fig. 2 of Ding et al. (2022) or Fig. 4 of Stone et al. (2023)).

We distinguish two main categories of residuals. First, the surface brightness of L1 is not accurately reproduced by the model close to the center of the galaxy and beyond the arc in the norther part of the cutout (see Appendix A.1). Second, the brightest part of the southern arc (corresponding to the very center of the source galaxy), as well as the compact feature (almost point-like) at the north of L2, are not fully captured by the source model. While the southern part leads to mild residuals only in F444W (below the 3σ level), the compact feature leads to strong residuals (more than 6σ within some pixels) with some symmetric features. In the source plane, this clump is clearly offset and distinct from the center of the source galaxy, as shown in the rightmost panel of Fig. 1. We believe this clump is resolved (as opposed to a point source), because increasing the source model resolution allows us to capture its extent over several pixels. We discuss in more detail this specific feature in Sect. 4.

The multi-band model of the background galaxy reveals a heavily wavelength-dependent morphology. In F150W and F200W filters, most of the detected regions of the source are located outside the main astroid (a.k.a., tangential) caustic. Interestingly, the morphology in these filters do not reveal any significantly bright component that could be associated to a centroid. It is only in F277W and redder bands that we see a more symmetric morphology containing features that could be attributed to a brighter central bulge, dust attenuated areas, or regions with lower stellar density. Moreover, our model reveals new features located south of the bulge, which may be associated to spiral arms. The source S/N is, as expected, higher along the caustics, because these regions are highly magnified and have at least two multiple images visible in the data. The bulge of the source galaxy is the highest S/N region and is located remarkably close to the southern part of the main tangential caustic (which features a double-cusp shape). Coincidentally, the upper part of the source crosses the northern cusp of the same caustic. Overall, the source S/N is larger inside and along the caustics, but is not significantly lower outside (as one may expect). We attribute this globally uniform S/N to the significant brightness outside the caustics in the mid-infrared, which effectively leads to higher S/N at these locations.

Our source S/N maps also allow us to discard highly uncertain source plane features, such as the smooth blob located around $(-27\rlap{.}{''}8, -5\rlap{.}{''}6)$. These spurious features are in reality caused by the leakage of un-modeled lens light features that contaminate the source model. Indeed, the purely smooth light model of L1 is inaccurate in some locations that overlap with the arc mask, causing the lensed source model to predict non-zero flux along the edge source plane grid. However, the posterior uncertainty of the source pixels is large, as expected. We expect that a better model of the deflectors surface brightness will remove these low-significance features from the source model. While a more flexible deflectors light model may be warranted in the future, our current model does not support the hypothesis of possible over- or under-subtraction of deflectors light over the arc mask region (i.e., all additional amplitudes varied over the arc mask region in each band remain extremely low $\lesssim 10^5$ e⁻/s).

While designing the arc mask, we noticed one luminous structure on the West side of the arc around image plane position $(2\rlap{.}{''}8, -0\rlap{.}{''}7)$ appearing bluer than the rest of the arc in the NIR-Cam data. This color difference may be the sign that this structure does not belong to the source, but is located along the line-of-sight instead. However, due to its close proximity with the arc and the absence of objective evidence that it does not belong to the source, we did not mask it and thus allow our source model to capture it. The unlensed version of this structure is clearly visible in the fourth column of Fig. 7 as a thin elongated feature of size $\sim 0\rlap{.}{''}1$ around position $(-26\rlap{.}{''}4, -5\rlap{.}{''}2)$. We note that Kamieneski et al. (2023) also did not mask this structure and ray-traced it to their source plane model (visible on the top right panel of their Fig. 2). Moreover, this structure being faint in the data, it has likely a small mass which may explain why we do not see signs of local distortions in the arc.

5.2. Critical lines and caustics

We compare in Fig. 8 the critical lines and caustics predicted by our three lens model families. All models predict qualitatively similar critical lines, with a characteristic feature around model position $(0'', 1'')$, on the East of L2. Overall, all models are consistent to each other in the vicinity of the lensed arcs, as expected from the many pixels that contain significant source flux. Nevertheless, we note several features that differ among the models. First, the critical lines from the "Cluster only" model do not extend towards L3, which is because this model converges to an Einstein radius $\theta_{E,L3}$ consistent with no mass, despite the prior from the measured stellar velocity dispersion. The critical line resulting from this model also shows a slight deviation outwards, which may be compensating the lack of mass on the east side of L1. Comparing the two models including external shear, we notice slight differences in the critical lines in between L1 and L3 and around L3, which are locations that are less constrained by strong lensing and mostly informed by the prior on the mass of L3 from stellar kinematics. Finally, due to the absence of an explicit cluster mass in the model, the caustics—and thus, the source position—in the "Shear only" model largely differ from the two other models. Indeed, the absence of large deflection fields from *El Gordo* leads to the source position being almost aligned with the deflectors, consistent with the observation of strong lensing features. Nevertheless, we note that the absolute source position is generally irrelevant (especially in cluster-scale regime) since numerous unobserved massive structures along the line of sight can shift the position of the source; hence, only relative positions of source intensity reconstruction relative to caustics are relevant.
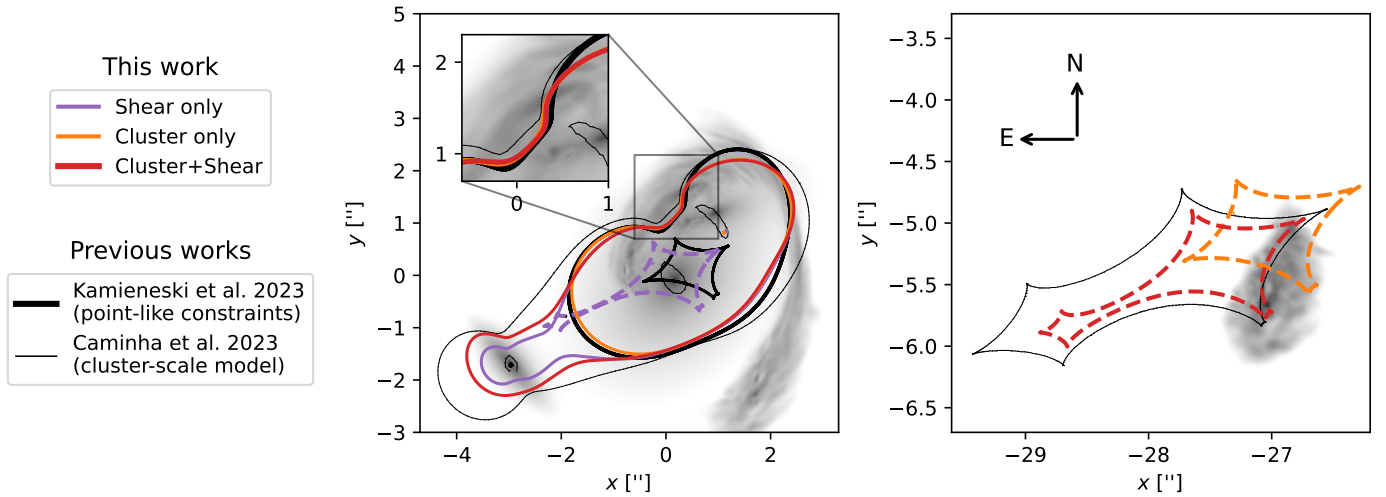
Fig. 8. Critical curves and caustics predicted by the different lens models explored in this work, namely "Shear only", "Cluster only" and our fiducial model "Cluster+Shear" that best fits the data. Also shown are the critical lines and caustics from recent models of *El Anzuelo*, namely from Kamieneski et al. (2023, constrained by pairs of multiple images with JWST imaging data) and Caminha et al. (2023, cluster-scale model of *El Gordo* using HST and MUSE data sets). Caustics from our models are shown with dashed lines for clarity. The left panel is focused on the image plane, while the right panel is focused on the source region predicted by models including the cluster mass distribution. Note how the position of the caustics for the "Shear only" model is aligned with the lens (left panel), compared to the caustics of other models (right panel). The predicted (unlensed) surface brightness of the lens and source galaxies from the best-fit "Cluster+Shear" model (red curves) is shown in the background, and North and East directions are indicated by the arrows.

In source plane, the tangential caustic have very distinctive features, caused by the combination of individual astroid caustics from the three main deflectors. These features—which are typical of binary or more complex lenses—have been studied in the past with catastrophe theory by describing complex caustic patterns as the product of so-called metamorphoses and critical points (e.g., Schneider & Weiss 1986). The eastern part of the caustic, towards the left in the right panel of Fig. 8, is dominated by the astroid caustic from L3. More towards the middle, we see a narrowing of the caustics, which is a consequence of a so-called beak-to-beak metamorphosis (see e.g., Orban de Xivry & Marshall 2009, second row of their Fig. 2). The western part of the caustics network corresponds to the merging of L1 and L2 astroid caustics. The southern cusp of these merged caustics is itself composed of two cusps, which is again a typical feature of binary lenses similar to a beak-to-beak transition. According to the classification of Shin & Evans (2008), these merging cusps features can be related to a Type 1 morphology, which in image plane is directly linked to the "dip" visible in the northern part of the critical lines around model position $(0'', 1'')$ (see second row of their Fig. 1). The critical lines are also very similar to those shown in Fig. 3 of Bozza et al. (2020, their $m = 0$ case). We note that this split cusp structure is visible in all lens models shown in Fig. 8 and, coincidentally, the brightest component of the source galaxy visible in the all NIRCam LW filters lies very close to it in source plane.

Although using pairs of multiply imaged features as constraints, the lens model of Kamieneski et al. (2023) is qualitatively very similar to ours. We show their critical lines and caustics[10] in comparison to ours in Fig. 8. As expected, the main differences in the critical lines are directly related to the amount and

location of the multiple images used in Kamieneski et al. (2023). A striking example is the westernmost part of the arc—around position $(2''.2, 1'')$—, for which Kamieneski et al. (2023) used a pair of multiple images which are probably unresolved by JWST and appears as point sources (images 2b and 2c in Fig. 11). In between these two images, all critical lines are overlapping, showing that both the arc and point-like constraints *locally* give similar results, despite our extended source model not including any point source components. On the contrary, in locations where either pairs of images are missing (e.g., south-western part of the arc) or inaccurate multiple images are used (northern part of the arc), clear differences do arise. In particular, the zoom-in inset in Fig. 8 focuses on a region with many multiple images of central regions of the source galaxy and shows deviations between the critical lines from different models. As we discuss in more detail in Sect. 5.4, we find that one feature in the arc may have been incorrectly attributed to a lensed image of the bright source bulge. We believe that this incorrect attribution causes the deviation between critical lines in the top right corner of the inset in Fig. 11, despite a region with a large number of lensing constraints. Focusing now on the caustics, we see a clear offset in the main astroid caustic between the model of Kamieneski et al. (2023) and our "Shear only" model. This result may be surprising at first, since both models are similarly parametrized (power-law profiles embedded in an external shear). However, this offset could be explained by the fact that our models including external shear all predict a non-zero mass for L3, as well as differences in the lensing constraints between the two approaches.

We also compare in Fig. 8 our critical curves and caustics to the ones predicted by the cluster model. The cluster model was constructed without any constraints from *El Anzuelo* hence L1, L2 and L3 are mainly constrained through scaling relations based on their photometry (Caminha et al. 2023). We find that critical lines between our galaxy-scale model and this cluster-scale overall agree well, in particular in the vicinity L1 and L2. As shown in the inset of Fig. 8, the characteristic feature in the

---

[10] An offset of $+0''.25$ E, $+0''.01$ N have been added to the critical lines and caustics of Kamieneski et al. (2023) for proper comparison with our models (P. Kamieneski, private communication). We have also found a similar offset between deflectors positions reported in Caminha et al. (2023) and our fitted light profile positions.

critical lines is comparable, meaning that qualitatively, the relative masses of L1 and L2 are consistent among the models. The cluster model displays rounder critical lines than our model, as expected from the use of spherically symmetric mass profiles. The discrepancy is the largest in the vicinity of L3, as this galaxy lies further away from the arcs. The cluster mass model assigns a larger mass to L3, which is also visible in source plane, where the eastern astroid caustic is significantly larger than in our models.

5.3. Constraints on mass model parameters

In this section we present our quantitative constraints on the mass distribution of the main deflectors. We show in Fig. 9 the joint posterior distributions of a subset of key mass model parameters, for each of the three model families (see Appendix A.2 for the full corner plot). We also summarize in Table 2 all constraints on mass model parameters for the fiducial "Cluster+shear" model. As expected, the Einstein radius of L1 and L2 as well the external shear strength significantly decrease after including the cluster mass distribution. Unlike the model of Kamieneski et al. (2023) composed of SIE profiles embedded in an external shear (which is the most similar to our "Shear only" model) the mass of L3 is constrained by the imaging data, except for the "Cluster only" model family. Our fiducial model predicts $\theta_{E,L3} = 0\farcs32 \pm 0\farcs03$, which is $\sim 3\sigma$ away from the stellar kinematics estimate $\theta_{E,SIS} = 0\farcs49 \pm 0\farcs05$. Therefore, the prior from stellar kinematics appears rather unconstraining compared to the imaging data, despite the angular distance between L3 and the lensing features.

In terms of the radial mass density profiles of L1 and L2, all model families predict logarithmic density slope values steeper than isothermal. Our fiducial "Cluster+Shear" model predicts density slope values of $\gamma_{L1} = 2.23 \pm 0.05$ and $\gamma_{L2} = 2.21 \pm 0.04$. These values are inconsistent with an isothermal slope at the $\sim 5\sigma$ significance level. We also note the anti-correlation between the density slopes of the two deflectors from the joint $\gamma_{L1} - \gamma_{L2}$ posterior distribution in Fig. 9. In Sect. 6.1 we discuss further these density slope constraints and place them in the broader context of galaxy evolution.

We compare our constraints on the mass distribution to those on the lens light distribution in order to detect possible offsets between the two components. We do so by showing in Fig. 10 a simplified view of the morphology of L1 and L2. The mass ellipticity of L1 is slightly larger than its luminous counterpart. While the orientations of the light and mass distributions of L2 are similar, those of L1 are slightly offset from each other, and the surface brightness of L1 seems to be oriented towards L2 more than its mass density. From Fig. 10 we also notice that the position angle of L1 is less constrained than for L2. This is not entirely surprising since the latter appears closer to the lensing features. Moreover, we find that the mass centroids of L1 and L2 are offset by about 3σ from their corresponding light centroids. More specifically, the center of mass of L1 is offset towards L2, while the one of L2 is offset towards the North-East. These offsets may be attributed to signs of gravitational interaction between the two galaxies. These differences in axis ratio and position angles are also visible in the full posterior distribution shown in Fig. A.2.

In Appendix A.3 we extensively check the robustness of our constraints against different modeling choices. These checks include the choice of VI sampler, the effect of inaccurate lens light model and the uncertainty associated to the cluster-scale model. In particular, we note that our models very weakly dependent on the source resolution, both in terms of constraints on mass model

parameters and morphology of the reconstructed source. We believe this low dependence on the source resolution is a direct consequence of the efficient regularization of our correlated field source model, which allows us to reach high-resolution without compromising on computation time and model quality.

Finally, we find our lens model to be sensitive to changes in the cluster-scale mass distribution, as drawing different posterior samples from the cluster model of Caminha et al. (2023) lead to measurable changes in χ^2_ν. In particular, some posterior samples from the cluster model lead to a lower χ^2_ν than with the best-fit cluster model we use in our fiducial model. Therefore, the *El Anzuelo* lensing features may be used to discriminate between different cluster models, thus providing additional constraints on the mass distribution of large-scale components of *El Gordo* (i.e., its dark matter halo). Although this particular result demands further investigation, it shows that extended arcs, although primarily constraining the structure of individual cluster members, may also provide useful constraints on the mass distribution at the scale of the cluster.

5.4. Lensed image families and clumps in the source

As the *El Anzuelo* lens system is composed of multiple deflectors and is directly influenced by its host cluster, it is not straightforward to assign a lensing origin to each individual feature observed in the arc. We use our fiducial lens model to show in Fig. 11 a set of multiply lensed images that correspond to prominent features either visible in the observed arcs or in the unlensed source model. Within a given image family, the lensed images are sorted according by increasing Fermat potential, or equivalently by their arrival time (Schneider 1985). For image families that were previously mentioned in Kamieneski et al. (2023), we try to follow as closely as possible their original numbering. This is the case for our image families 1 (left column of Fig. 11), and 2 and 3 (right column). However, since we provide more multiple images per image family—and we find that image 1b from Kamieneski et al. (2023) does not belong to family 1—the specific letter used in image identifiers must differ from theirs. Diego et al. (2023) also refers to three families of multiple images, although without explicit identifiers (see their Fig. 2). We note that, for all image families shown in Fig. 11, the lens equation also predicts images appearing at the position of L1 and L2. These are extremely demagnified images (given the cuspy nature of power-law profiles with super-isothermal slope). We do not show these central images in order to avoid cluttering the figure.

We are able to confirm that parts of the background galaxy are multiply imaged five times (excluding central images); in Fig. 11 this is shown by image families 1 and 3. This peculiar lensing configuration has been first suspected in Kamieneski et al. (2023). We check if these fifth images are magnified by computing their model-predicted magnification from our fiducial mass model. We obtain magnifications of $\mu \approx -3$ for image 1d and $\mu \approx -5$ for image 3b, thus we find there are magnified. We note that this "exotic" lensing configuration typically arises in systems with multiple deflectors and has been the topic of several theoretical works in the past (e.g., Shin & Evans 2008; Orban de Xivry & Marshall 2009; Bozza et al. 2020). We briefly discuss in Appendix A.4 potential implications regarding this lensing configuration.

We find that one of the images used in Kamieneski et al. (2023) as being part of the image family 1 (their image 1b) in fact does not belong to this set of multiple image according to our lens model. On the one hand, we find that their image 1d
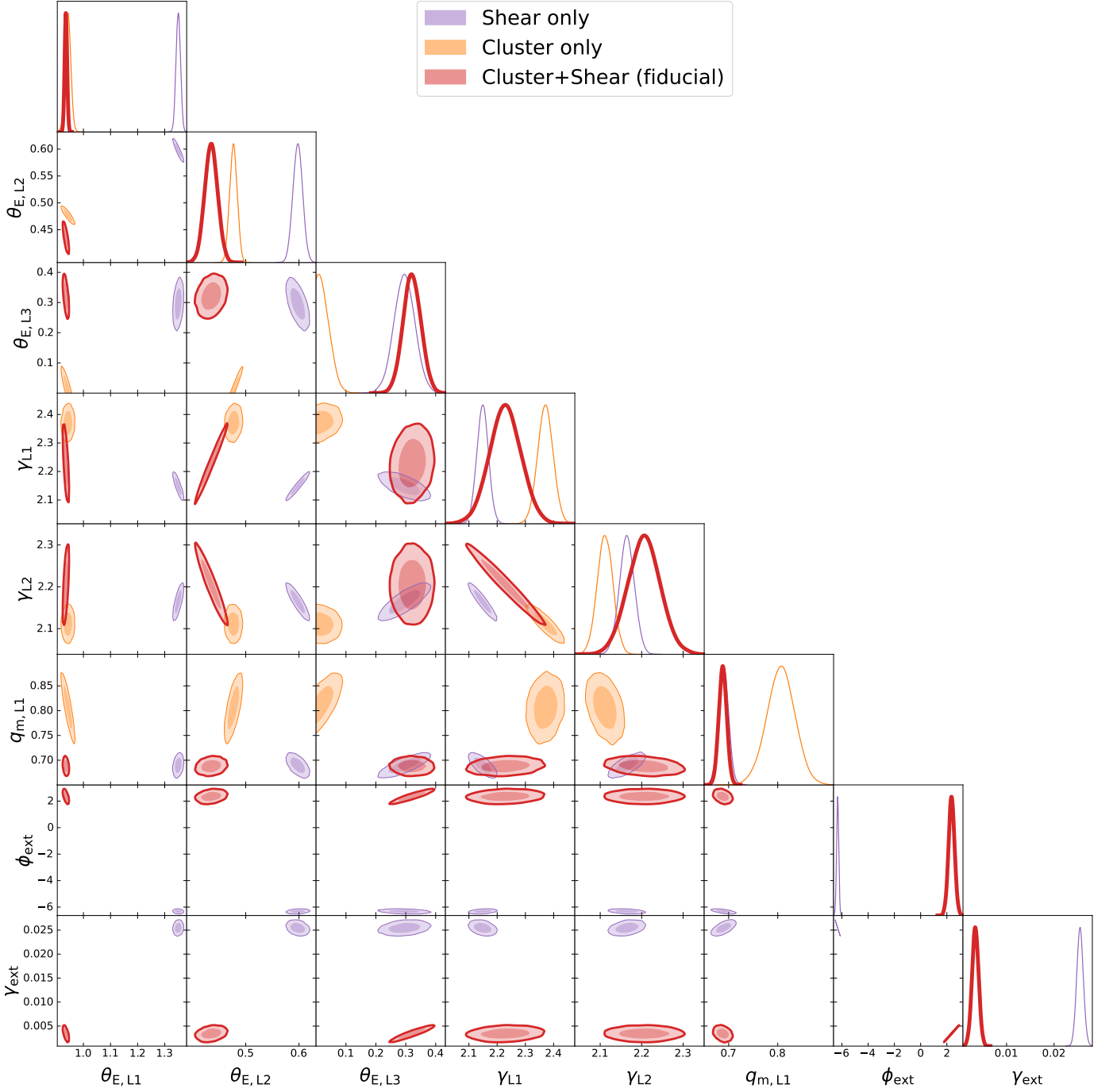
Fig. 9. Joint posterior distribution of a subset of lens mass parameters, for the 3 main model families tested in this work. The first one includes only external shear in addition of the three main deflectors, the second one replaces external shear with the *El Gordo* cluster deflection field, and the last one includes a combination of the two. The parameters shown in the figure are the Einstein radii ($\theta_{E,L1}$, $\theta_{E,L2}$, $\theta_{E,L3}$), the logarithmic density slopes at θ_E (γ_{L1}, γ_{L2}), the mass axis ratio ($q_{m,L1}$), and the external shear orientation and strength (ϕ_{ext}, γ_{ext}, when included in the model). See Fig. A.2 for the full mass model parameters space.

is in fact composed of the two images denoted by 1a and 1c, which appear like merging while crossing the tangential critical line. On the other hand, their image 1b corresponds to our image 4a in Fig. 11, and thus originates from a distinct compact bright clump in the source, located at the north of the central bulge. We note that this clump has similar colors as the bulge of the source galaxy, which is why it could have been incorrectly attributed to a lensed image of the bulge. Interestingly, not all images of this clump are visible in the data. We believe it is mostly

due to a combination of a the larger FWHM of the PSF in redder bands, and stronger contamination by the deflectors light. To better visualize this, we show in Fig. 12 a comparison between our the lensed and convolved source model and the corresponding model before convolution by the PSF (in F356W although it is similar in other filters). We see that only image 4a remains clearly visible after convolution. Moreover, the lensed images appear either close to the bright bulge of the source (image 4d), or close to regions heavily contaminated by the deflectors light

Table 2. Constraints on the mass distribution of the main deflectors.

Mass component / Parameter	θ_E [″]	γ	q_m (or γ_{ext})	ϕ_m (or ϕ_{ext}) [deg]	x_m [″][†]	y_m [″][†]
L1 (EPL)	0.935 ± 0.005	2.23 ± 0.05	0.69 ± 0.01	37.7 ± 4.7	0.163 ± 0.004	-0.08 ± 0.01
L2 (EPL)	0.44 ± 0.01	2.21 ± 0.04	0.72 ± 0.01	22.7 ± 1.6	0.89 ± 0.01	1.172 ± 0.004
L3 (SIE)	0.32 ± 0.03	$2.00^\star$	$0.60^\star$	$-0.86^\star$	$-2.97^\star$	$-1.69^\star$
External shear	—	—	0.003 ± 0.001	2.4 ± 0.2	—	—
Host cluster	Model from Caminha et al. (2023) without L1, L2, L3					

Notes. The above constraints are computed from the marginalized posterior distributions of our fiducial "Cluster+Shear" model.
[†] The origin $(0'', 0'')$ of our model coordinate system coincides with WCS coordinates $(15.7057851°, -49.2518014°)$, the x axis is positive towards the West and the y axis is positive towards the North.
[★] Except for θ_E, all L3 parameters are fixed to an isothermal slope ($\gamma = 2$) or to values informed by the surface brightness model.
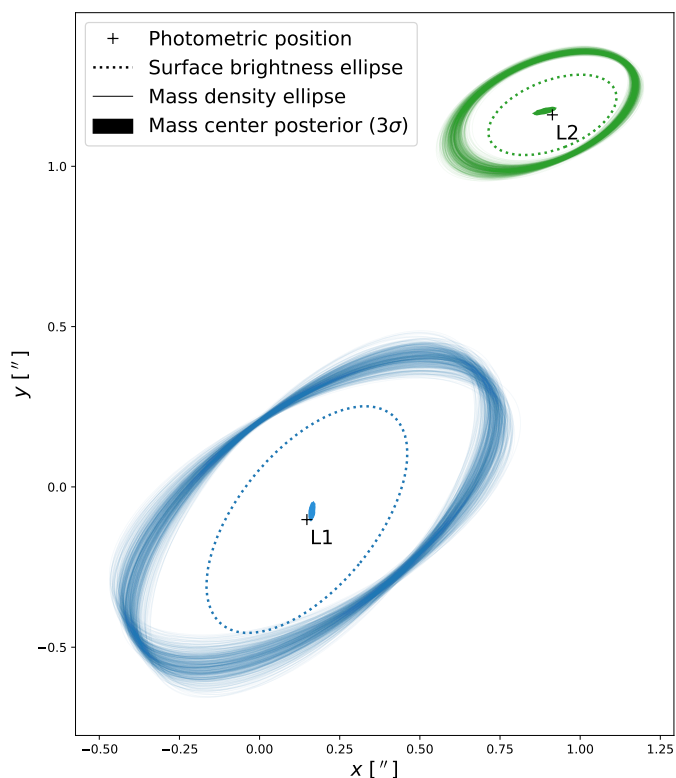

Fig. 10. Visualization of position, ellipticity and angular size of the deflectors L1 and L2. For each galaxy, the cross shows the mean position across the six bands from the fit to the surface brightness (double-Sérsic profile), and the dotted line shows an ellipse to visualize that fit whose radius corresponds to the half-light radius of the profile. The sets of thin lines are ellipses corresponding to 500 individual samples of the lensing convergence (EPL profile) with radius equal to the Einstein radius, drawn from the posterior distribution of Fig. 9. Close to the position of each deflector, small shaded contours indicate the posterior distribution of the EPL center (extending to 3σ). For each deflectors, we see offsets in position angle and centroids between their mass and light distributions.

(images 4b and 4c); therefore, they are not seen in the data. From one of our a higher resolution source models (with $n_{src} = 300$), we estimate that the physical size of the clump is approximately 400 pc at redshift $z_s = 2.291$. While this estimate is an upper-bound to the true size—since increasing the source resolution tends to make it more compact—this clump in the source is remarkably small. It is comparable in size to some of the structures

in the jets of lensed sources analyzed in Powell et al. (2022) using VLBI observations with milli-arcsecond resolution (against 30 milli-arcsecond resolution with JWST/NIRCam data).

Finally, we note that our extended source model can be used to extract the spectral energy distribution (SED) of compact unresolved structures in the arc. We show in Appendix B the case of one of the brightest point-like feature in *El Anzuelo* (image 2b in Fig. 11). As our pixelated source model, at its fiducial resolution ($n_{src} = 100$), does not capture unresolved features by construction, it can be directly subtracted from the data to separate the extended source component from these unresolved features. It is then easier to perform photometric measurements and estimate the SED of such compact source regions, which are important tracers of the star formation history (as shown in Kamieneski et al. 2023).

5.5. Summary of the main findings

One of the main results of our strong lensing analysis of *El Anzuelo* is the measurement of mass density slopes of the cluster member galaxies L1 and L2 at redshift $z \approx 0.9$. We find that both deflectors, especially the lower mass galaxy L2, have density profiles steeper than isothermal from 3σ to 9σ statistical significance. These constraints are obtained by modeling the full surface brightness of the lensed dusty galaxy, for which we detect and reconstruct a small luminous clump of size $\lesssim 400$ pc at redshift $z \approx 2.3$. We discuss in more details these findings and place them in a broader context in Sect. 6.

5.6. Release of lens models within the COOLEST standard

Previous sections describe our modeling and inference approach with a level of details that aim at maximizing the reproducibility of our analysis. With this idea in mind, we also publicly release all lens models[11] following the strong lensing standard COOLEST (Galan et al. 2023). These models can then be easily loaded using the Python package `coolest`[12] for further analyses, in particular with any modeling codes that share an interface with COOLEST (see the documentation for a list). We encourage future lens models to be released under this standard, in order to facilitate comparison with the present analysis.

---

[11] Lens models under the COOLEST format will be released at the publication of the article, although they can be shared earlier upon reasonable request.
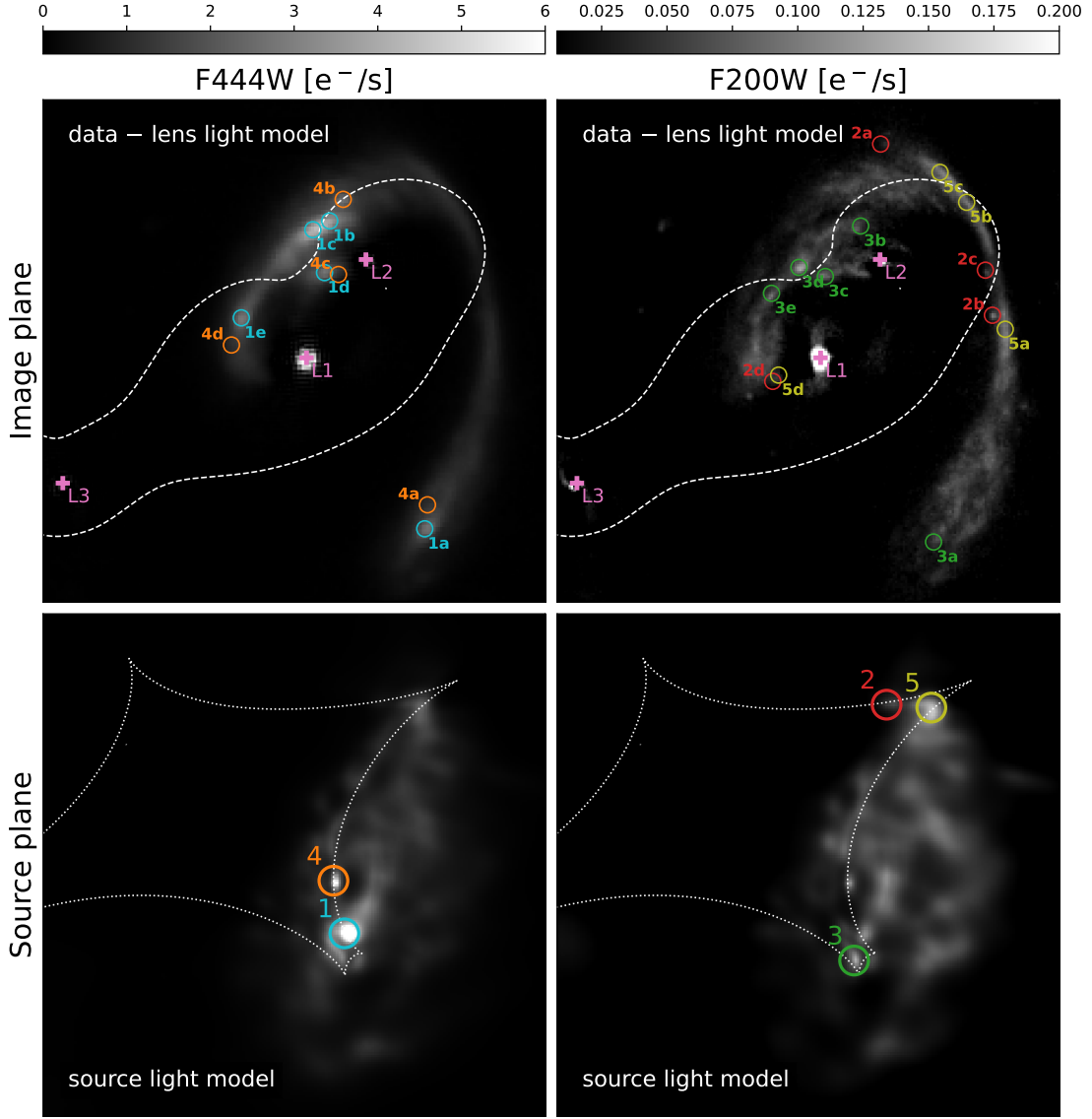[12] https://github.com/aymgal/COOLEST

Fig. 11. Multiple images of peculiar features in the background source galaxy. *Top row*: families of multiple images in image plane together with the critical lines and the observed flux from the arc (after lens subtraction in filters F444W ad F200W). Also shown are the positions of the three deflectors with pink crosses (residuals remaining after lens light subtraction are visible around L1 and L2 positions), as well as the critical lines with dashed white lines. Our model also predicts images at the position of L1 and L2, although there are not shown here to limit clutter. *Bottom row*: corresponding image positions on the source plane, superimposed onto one sample of our source model. The tangential caustic is shown with dotted white lines. Note that each column has its own dynamic range.

6. Discussion

6.1. Mass density profile of elliptical galaxies

Gravitational lensing allows us to understand the interplay between dark matter and baryons, and how this interplay shapes the inner structure of galaxies and galaxy clusters. Strong lensing in particular probes the two-dimensional mass distribution of galaxies via the enclosed mass within the Einstein radius θ_E and—when high S/N extended arcs are used—the radial density slope measured at θ_E. Different processes can impact the density slope, such as the cooling of baryonic matter followed by dark matter halo contraction (e.g., Gnedin et al. 2004; Abadi et al. 2010), itself compensated for by outflows from stellar winds or AGN feedback (e.g., Johansson et al. 2012; Dubois et al. 2013). Large elliptical galaxies, which are prevalent of cluster-scale and galaxy-scale strong lenses, were found to have a radial behav-

ior remarkably close to an isothermal profile (i.e., $\gamma = 2$) from lensing and lens stellar dynamics constraints (e.g., Treu & Koopmans 2002; Auger et al. 2010; Sonnenfeld et al. 2013). This result has been termed the "bulge-halo conspiracy" in the literature (Treu et al. 2006; Dutton & Treu 2014; Etherington et al. 2023a): despite the different radial behaviors of baryonic and dark matter profiles, their combination seems to lead to an isothermal density profile, with no evident signs for evolution with redshift (e.g., Sonnenfeld et al. 2013; Etherington et al. 2023a). At the population level, this result has been recently confirmed using lensing-only constraints, larger samples, and more modern lens modeling techniques (Shajib et al. 2021; Etherington et al. 2022; Tan et al. 2023).

The three foreground deflectors if *El Anzuelo* have typical photometric signatures of elliptical galaxies, and have been confirmed to be members of the massive cluster *El Gordo* (e.g., Caminha et al. 2023). In this work, we model the mass distri-
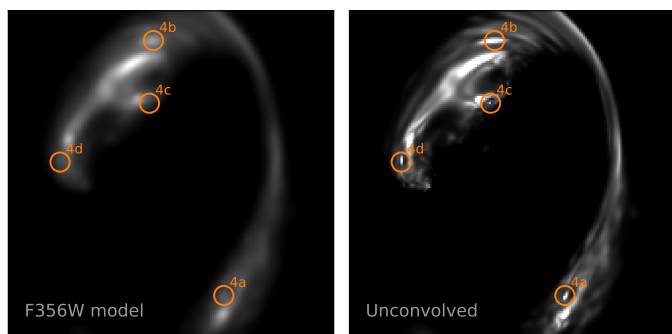
Fig. 12. Multiple images of a ≲ 400 pc compact clump in the source galaxy (image 4 in Fig. 11 and shown in color in Fig. 1). Only image 4a is clearly visible in the data and our model, shown in the left panel (shown here for filter F356W, which also looks similar in F277W, F410M and F444W filters that are not shown). The right panel shows for comparison the model before convolution by the PSF, which reveals the four multiple images (the colormap slightly saturates the brighter pixels to improve contrast).

bution of these galaxies using elliptical power-law profiles perturbed by the cluster mass distribution and an additional external shear. As presented in Sect. 5 (Table 2), we infer logarithmic density slopes for L1 and L2 of $\gamma_{L1} = 2.23 \pm 0.05$ and $\gamma_{L2} = 2.21 \pm 0.04$, respectively. These values are inconsistent with an isothermal slope, and γ_{L2} is 2.7σ away from the mean value $\langle \gamma \rangle = 2.075 \pm 0.024$ of Etherington et al. (2023a) inferred from a subset of SLACS (Bolton et al. 2006) and GALLERY (Shu et al. 2016) systems. As detailed in Sect. 4, we infer our uncertainties by marginalizing over an ensemble of model variations with Bayesian weighting. We also looked for potential systematic effects and did not find statistically significant changes in the posteriors distributions by running additional models. Here, we first compare the precision of these measurements with previous analyses of similar imaging data, then discuss the possible origins of these results in terms of galaxy structure.

Two galaxy-scale strong lenses observed in multiple NIR-Cam filters have been analyzed at the time of writing this manuscript: the backlit-galaxy system VV 191 from the PEARLS program (Keel et al. 2023) and the dusty strongly lensed galaxy SPT0418−47 from the TEMPLATES program (Cathey et al. 2023; Rüstig et al. 2024). For both of these systems however, the data quality and lensing features are not comparable to the PEARLS observations of *El Anzuelo* (almost no counterimage for VV 191, small separation and low S/N for SPT0418−47). Moreover, the density slope parameter has been fixed to the isothermal value in both analyses. Therefore we turn to analyses of multi-band imaging data from HST instead, acknowledging that those are usually based on a smaller number of filters. One example is the semi-automated modeling effort of Tan et al. (2023), where the authors jointly fit between 1 and 3 HST filters[13] in the visible and ultraviolet wavelengths for a selection of SLACS and SL2S systems. The average uncertainty on the density slope is 0.03 (without their additional systematic error term and for SLACS systems only, as those have overall higher S/N than SL2S) which, reported to our mean value for L1 gives to a relative precision of 1.4%. This relative precision is smaller than ours (2.2% and 1.8% for L1 and L2, respectively), despite our lens model being constrained by 6 filters at higher

resolution. This gives further confidence that our uncertainties on γ are not under-estimated, since they are larger than those typically obtained with typical HST strong lensing data.

That elliptical galaxies have nearly isothermal radial density profiles in their inner region has been observed in isolated deflectors, such as those from the SLACS (Bolton et al. 2006) and SL2S (Gavazzi et al. 2012) samples. The three main deflectors of *El Anzuelo* are, however, not isolated but genuine members of *El Gordo* that are gravitationally interacting. Therefore, it may not be surprising to measure density slopes that deviate from an isothermal profile. For most of isolated lens systems from SLACS (or comparable samples) we note that the ratio $\bar{r}_{E/eff}$ between the Einstein radius and the half-light radius, $\bar{r}_{E/eff} \equiv \theta_E / \theta_{eff} \lesssim 1$, meaning that lensing overall constrains the inner region of the lens galaxies, within their half-light radius (e.g., see the middle panel of Fig. 15 from Etherington et al. 2022, for SLACS and GALLERY samples). For the case of *El Anzuelo*, L1 and L2 both have $\bar{r}_{E/eff,L1} \approx 1.6$ and $\bar{r}_{E/eff,L2} \approx 1.3$ respectively (as visualized in Fig. 10), meaning that lensing provides constraints at overall larger radii compared to lens galaxies from the aforementioned samples[14]. The main reason for *El Anzuelo* deflectors to have $\bar{r} > 1$ is that their apparent lensing effect is boosted by the mass density of the host cluster, leading to the appearance of an Einstein ring that is larger than if L1 or L2 were isolated galaxies. This effect can be qualitatively confirmed by noting the difference in θ_E values between the "Shear only" and "Cluster+Shear" models (e.g., Fig. 9): including the cluster mass distribution in the model significantly reduces θ_E values for L1 and L2 in order to fit the imaging data. Therefore, the observed lensing features probe the mass distribution of the deflectors at sensibly larger radii, compared to isolated deflectors.

Beside larger Einstein radii in the vicinity of their host cluster, it has been shown that cluster members are expected to have truncated radial density profiles, in particular in the low to intermediate mass range (e.g., Natarajan et al. 2002; Monna et al. 2015). Truncated mass distributions typically arise in cluster environments as a result of tidal stripping. Recently, Granata et al. (2023) discuss opportunities and challenges that exist when constraining the truncation radius r_t and central velocity dispersion σ parameters of cluster members. In the case of *El Anzuelo*, it is interesting to estimate a range of plausible truncation radii expected for deflectors L1 and L2. We can do so by looking at the $r_t − \sigma$ relation summarized in Fig. 11 of Monna et al. (2015). For a velocity dispersion $\sigma_{L1} \approx 300$ km s^{-1} for L1 ($\sigma_{L2} \approx 200$ km s^{-1} for L2), the truncation radius is expected to fall in the range $10 − 100$ kpc ($8 − 70$ kpc). The circularized Einstein radius in physical units r_E inferred from our lens model is $r_{E,L1} \approx 7$ kpc ($r_{E,L2} \approx 3$ kpc), likely smaller than the truncation radius. However, the asymmetric arcs of *El Anzuelo* extend to a maximal projected distance of ~ 40 kpc for L1 (~ 15 kpc for L2), that is within the range of plausible truncation radius values. Therefore, it may be possible to constrain the truncated profile of these cluster members from extended source modeling, especially for L2 due to its smaller size. In the same study, Granata et al. (2023) also mention that r_t and σ are degenerate (see also Bergamini et al. 2019), and discuss how different methods and observables help mitigating this issue. In particular, they make the parallel between two types of lensing analyses: (1) point-like multiple images appearing close to cluster members over a possi-

---

[13] The system SDSS J0912 + 0029 is the only system modeled using 4 filters, but is excluded from their analysis due to high lens light contamination and low S/N for the arcs.

[14] The effective radius for L2 may be underestimated due to due blending with the lensed arcs (see Appendix A.1). However, due to the lensing boost by the cluster, the ratio $\bar{r}_{E/eff,L2}$ is likely larger than unity.
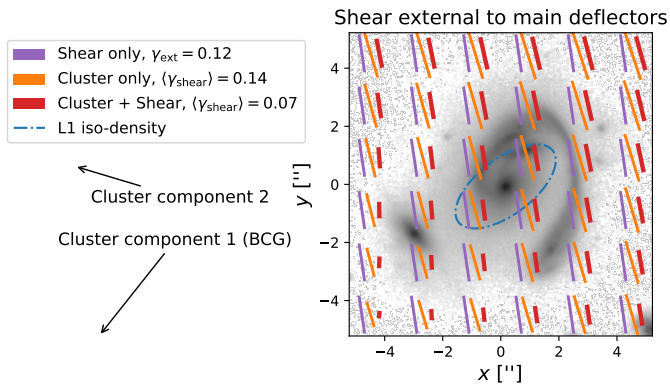
Fig. 13. Shear orientation and strength over the field of view of *El Anzuelo*. For the "Shear only" model, the shear field is a uniform external shear with strength γ_{ext}; for the "Cluster only", it is the shear field from the cluster model of Caminha et al. (2023); for the "Cluster+Shear" model, it is the combined effect from the uniform external shear and the cluster shear. For the latter two models, the averaged shear strength $\langle \gamma_{shear} \rangle$ is also indicated the legend. The absolute length of the shear markers is arbitrary, but their relative size is respected. The blue ellipse indicates the orientation of the mass density of L1. On the left of the plot, we show the directions pointing towards the two main dark matter halo component of the *El Gordo* cluster. Note that the shear orientation is consistent with the position of the shear scale components.

bly large range of radii (as in Granata et al. 2023), and (2) single extended arcs warping around cluster members (e.g., as in Suyu & Halkola 2010; Monna et al. 2015). The particular case of *El Anzuelo* seems to bridge the gap between the two situations, as lensing features have both high S/N and a significantly assymetric shape, such that they cover a large range of galactic radii. In summary, *El Anzuelo* is a promising system to go beyond simple density profiles and possibly characterize tidal truncation, as suggested by the steep density profiles we infer.

Finally, we note that measurements of a single mass density slope from lensing may be affected by systematic biases caused by simplistic modeling assumptions (e.g., Sonnenfeld 2018; Kochanek 2020; Cao et al. 2022). If the intrinsic radial profiles of the deflectors are more complex (e.g., with one or more inflection points), approximating those with a single power-law profiles can result in a biased interpretation of the constraints, either over- or under-estimating the slope depending on the location of the lensing features (e.g., Gomer & Williams 2020; Millon et al. 2020). In the case of *El Anzuelo*, the considerable thickness of the arcs and the very asymmetric lensing configuration—the northern arcs being significantly closer to L1 and L2 in projection—may provide constraints for a more flexible model, along both radial and azimuthal directions.

6.2. Can the host cluster be approximated by a constant external shear?

In most of galaxy-scale strong lensing analyses, the net effect of masses external to the main deflectors is usually approximated by a constant external shear field. Here we investigate further the assumption of a constant external shear, compared to the explicit spatially varying contribution of the cluster. To help visualizing the various shear fields at play, we compare the best-fit shear fields (that are external to L1, L2, L3) from our three model families in Fig. 13.

We are interested to verify if the host cluster *El Gordo*, at the position of *El Anzuelo*, could be modeled using an approxi-

mation. As reported in Sect. 5, we find that external shear alone leads to a better fit to the data compared to using the fixed deflection field of the cluster, with a χ^2_ν difference of > 0.02. This results may seem surprising: a constant external shear field—which remains a first-order approximation of the cluster's true shear field—leads to a better fit than the full cluster model. In other words, an optimizeable two-parameters approximation performs better than the more complex but fixed model. We argue that these result may in fact be expected: the cluster mass model is the most accurate in the vicinity of multiple image pairs used as constraints. Among the families of multiple images used to constrain the cluster-scale mass model, the closest images are located at approximately 15″ North-East from *El Anzuelo* (images 3b and 17c in Fig. 1 of Caminha et al. 2023). Further away from these constraints, the extrapolated model may be less accurate compared to the constraining power of the arc of *El Anzuelo*. On the contrary, the external shear with free parameters can adjust to this constraining data and lead to a better fit.

Our fiducial model combines the fixed cluster field with local corrections from an uniform external shear. We visualize the different external shear fields involved in Fig. 13, which also indicates directions towards the two cluster-scale dark matter halos of *El Gordo* (Caminha et al. 2023). We see that the shear from the cluster is mainly mainly driven by the position of the BCG. The uniform correction by the external shear has the net effect of re-orienting the shear direction more towards the second main component of *El Gordo*, which is located towards to the North-East of *El Anzuelo*. The fact that constraints from *El Anzuelo* allows us to locally correct the cluster-scale model is another hint that extended arcs are complementary to cluster-scale lensing observables.

6.3. Using extended arcs instead of point-like constraints

In this work we use the full information encoded in the arcs in multiple wavelengths to constrain the mass distribution of the deflectors. Compared to only using families of point-like images, pixel-level modeling has two main advantages: the risk of mistakenly assigning pairs of images that do not share the same physical origin is minimized, and the number of lensing constraints is maximized. In Sect. 5.4, we selected and labeled multiple compact regions in source plane and computed their corresponding multiple lensed positions. Similar to the concept of geometric redshifts (see e.g., Diego et al. 2023), we argue that our lens model is better at securing pairs of multiple images in the absence of a spectroscopic confirmation, compared to relying solely on color and morphological information. Strengthening this argument is the remarkable agreement between our model and the model of Kamieneski et al. (2023). Their model was built using point-like constraints such as the unresolved pair of images that we name 2b and 2c in Fig. 11. Our model predicts critical lines that pass in between the two images, *despite the feature being absent in our source model*, meaning that the extended arcs are at least as good as these two unresolved features to constrain the lens model at this location.

We compared in more details our results with the lens model of Kamieneski et al. (2023), especially for three image families. In their analysis, the authors used the 8 NIRCam filters to look for compact features in image plane that have consistent colors, and considered those as multiple images of same region in the source. For their image family 1, they used a simplified initial lens model to confirm the five-image configuration, interpreted as a confirmation of the origin of images 1a to 1e being lensed versions of the bright central region of the source galaxy.

In Sect. 5.4, we show that image 1b does not originate from the center of the source, but rather from an off-centered compact clump of size $\lesssim$ 400 pc. In NIRCam images, this clump has similar colors as the central bulge of the source (see Fig. 2 of Kamieneski et al. 2023), which is the reason why the only visible image of clump has been associated to the bulge in source plane. Consequently, we caution on using solely photometric signatures (shapes or colors) to draw conclusions on the lensing origin of features in the arcs. The use of incorrect pairs of multiple images is likely to bias the inference on the source morphology and mass model parameters. However, depending on the application and the required precision of the measurements, these biases may not always affect the conclusions of the analyses. In particular, the analysis of Kamieneski et al. (2023) is likely unaffected, as it focuses on large-scale properties of the source, such as the stellar mass, star formation rate and color gradients over kiloparsec scales.

6.4. Limitations and future improvements

While we present the most advanced model of *El Anzuelo* to date, our analysis relies on a set simplifying assumptions. Our strongest assumption is the modeling of the light and mass distributions with smooth elliptical profiles. The model residuals (see Fig. 7) reveal that the lens light distribution is more complex than what can be modeled with concentric Sérsic profiles, with possible signs of boxyness and tidal stripping due to the interaction between the three deflectors. If already visible in the light distribution, the underlying mass distribution is likely to be more complex than single elliptical power-law profiles, in particular requiring additional degrees of freedom in the radial and azimuthal directions. First-order deviations from the power-law profile can be added, for example, through multipoles (typically of order 3 or 4 (e.g., Van de Vyvere et al. 2022; Galan et al. 2022; Powell et al. 2022), cored and truncated profiles (e.g., Elías-dóttir et al. 2007) or broken power-law profiles (e.g., Du et al. 2020). Complexity in the lens light could be added similar to our source model, or using similarly flexible methods like sparsity and wavelet regularization (Galan et al. 2021). Jointly fitting the lens light with the other model components would add extra constraints to lens mass distribution, similar to so-called composite lens models in which the baryonic and dark matter components are modeled as separated profiles (as commonly used in lensed quasar cosmographic analyses, Suyu et al. 2014; Millon et al. 2020). We defer the use of more elaborate lens models to future works.

Regarding spectroscopic data, in this work we only attempt to extract the central velocity dispersion from the VLT/MUSE observations. Nevertheless it may be possible to measure the velocity dispersion at various locations around the center of L1 and L3, and perhaps properly separate the flux of L2 from L1. Additional measurements points could help constraining further the mass distribution of the deflectors, in particular L3 for which we find that a single velocity dispersion is less constraining that the lensing data. Spatially resolved kinematics measurements can also help mitigating degeneracies inherent to lens models (e.g., the mass-sheet degeneracy, Treu & Koopmans 2002; Schneider & Sluse 2013; Gomer et al. 2023; Shajib et al. 2023). Using stellar kinematics of the lensed galaxy can also mitigate model degeneracies, in addition to provide insights on the dynamical properties of *El Anzuelo* (Rizzo et al. 2018; Chirivì et al. 2020). However, extracting reliable measurements at the location of the arcs would require much deeper exposures than the present MUSE data.

Finally, we draw attention to the limited knowledge of noise characteristics in JWST data. Based on our model of *El Anzuelo*, we notice that noise levels seem over-estimated (alternatively, the exposure time under-estimated) in some locations. One can see in the central column of Fig. 7 that normalized residuals, in some regions within the arc mask, appear "flatter" than expected from pure random noise. This local over-estimation of the noise level may lead in turn to an over-estimation of parameters posterior uncertainties. Although for this reason we believe our main results are unaffected, we emphasize that it will be important to better characterize the noise statistics when modeling JWST/NIRCam pixels (not only for lens modeling analyses), in order to get reliable parameters uncertainties[15]. As shown by the PEARLS (Windhorst et al. 2023) and TEMPLATES (Rigby et al. 2023) programs, special care in the reduction of JWST spectroscopic and imaging data must be taken, in particular the challenging removal of $1/f$ noise patterns. These complex reduction steps make it challenging to fully control and understand the noise properties. We encourage future works to explore the impact of the noise properties on lens modeling analyses.

7. Summary and conclusion

In this work, we model in details the prominent strong lens system *El Anzuelo* in the vicinity of the massive cluster *El Gordo*. We do so using high-resolution and multi-band JWST/NIRCam imaging data obtained from the PEARLS program (Windhorst et al. 2023) and MUSE/VLT specstroscopic data (Caminha et al. 2023). This system is composed of three elliptical galaxies as main deflectors (L1, L2, L3) at redshift $z_d \approx 0.9$ and a strongly lensed dusty star forming galaxy at redshift $z_s \approx 2.3$. We summarize below the novelty of our analysis and its main results:

– We apply, for the first time on real data, the differentiable lens modeling code HERCULENS (Galan et al. 2022) to model the large number of NIRCam pixels. We combine HERCULENS with a novel three-dimensional source model and a variational inference approach using NIFTY.RE (Edenhofer et al. 2024). Our inference pipeline can run on both CPUs and GPUs, the latter allowing us to obtain approximate posterior distributions in about 2 hours, for $\sim 10^5$ model parameters constrained by $\sim 10^6$ data points.

– We measure the line-of-sight stellar velocity dispersion for two of the deflectors using VLT/MUSE data, and use these measurements to further constrain the mass of deflector L3. However, we find that the current precision on the velocity dispersion only marginally impacts the constraints from the lens models.

– We extensively compare our lens model based on extended source modeling to the analysis of Kamieneski et al. (2023) based on point-like constraints within the arc. We show a good qualitative agreement between the models, confirm the five-image lensing configuration and demonstrate how extended source modeling can be used to secure the nature of compact features in the lensed arcs. We caution on relying solely on color and morphology information, since it can lead to incorrect identifications of multiple images.

---

[15] Close to completion of this work, error maps ("_err" files) have been uploaded on the PEARLS website. We compared best-fit models and corresponding χ^2 values obtained using either our empirical uncertainty estimation or these error maps, and noticed that the latter lead to χ^2_ν values significantly lower than 1, especially in SW filters. Therefore, we choose to keep our noise maps based on estimated exposure maps.

- We find that cluster members L1 and L2, which create most of the strong lensing effect, have density slopes at Einstein radius steeper than isothermal with $\gamma \gtrsim 2.2$. We make the hypothesis that such steep density slopes are caused by two factors. (1) The lensing boost from the host cluster increases the Einstein radius, such that lensing features probe further away from the deflectors centroids. (2) The mass density profile of cluster members is tidally truncated, such that their measured density slopes can appear super-isothermal.

- We show that a uniform external shear field does not accurately approximate the cluster mass distribution over the field of view of *El Anzuelo*. Our best-fit lens model explicitly incorporates the cluster lensing contribution from the model of Caminha et al. (2023), and uses the external shear component to locally correct its deflection field over the field of view.

- Our high-resolution multi-band source model allows us to detect and locate a small luminous clump, with a maxmimal size of 400 pc at the source redshift. To our knowledge, this may be one of the first clumps of this size located in a dusty galaxy at redshift $z \sim 2.3$. Only one out of the four multiple images of the clump is visible in the data, but its detection is possible thanks to extended lensing constraints, color information and high resolution of JWST/NIRCam.

Photometric searches have already, and will continue to, provide new galaxy-scale lenses with prominent arcs like *El Anzuelo* in cluster environments (e.g., Jaelani et al. 2020; Garvin et al. 2022). Of the order of 10^5 new galaxy clusters are expected to be discovered from deep wide field surveys such as the one undertaken with the Euclid space telescope (e.g., Euclid Collaboration 2019; Natarajan et al. 2024), with likely similar numbers from the future Legacy Survey of Space and Time at the Rubin observatory. Such a large increase of known clusters will inevitably increase the number of galaxy-scale lensing events, which have so far been more numerous than predicted by ΛCDM (Meneghetti et al. 2022, 2023).

In the past, very few studies jointly used families of multiple images in galaxy group or cluster environments together with extended source modeling to improve constraints on the distribution mass and further probe the structure of galaxies (Monna et al. 2015; Wang et al. 2022). Other studies have used state-of-the-art source modeling techniques to assess the accuracy of cluster-scale lens models and visualize the morphology of background galaxies (e.g., Grillo et al. 2016, 2020), which is a step towards this goal. We have shown in our work that recent advances in forward modeling and inference techniques, boosted by GPU parallelization, enable pixel-level modeling of a large number of data pixels while maintaining low computation times. Therefore, it is within reach to expend strong lensing analyses of galaxy groups and clusters by incorporating extended arcs modeling in the near future.

References

Abadi, M. G., Navarro, J. F., Fardal, M., Babul, A., & Steinmetz, M. 2010, MNRAS, 407, 435

Abbott, T. M. C., Aguena, M., Alarcon, A., et al. 2020, Phys. Rev. D, 102, 023509

Acebron, A., Schuldt, S., Grillo, C., et al. 2023, A&A, 680, L9

Adams, N. J., Conselice, C. J., Austin, D., et al. 2023, arXiv e-prints, arXiv:2304.13721

Arras, P., Baltac, M., Ensslin, T. A., et al. 2019, ascl:1903.008

Arras, P., Frank, P., Haim, P., et al. 2022, Nature Astronomy, 6, 259

Astropy Collaboration, Robitaille, T. P., Tollerud, E. J., et al. 2013, A&A, 558, A33

Auger, M. W., Treu, T., Bolton, A. S., et al. 2010, ApJ, 724, 511

Bacon, R., Conseil, S., Mary, D., et al. 2017, A&A, 608, A1

Bayliss, M. B., Hennawi, J. F., Gladders, M. D., et al. 2011, ApJS, 193, 8

Bergamini, P., Rosati, P., Mercurio, A., et al. 2019, A&A, 631, A130

Bergamini, P., Schuldt, S., Acebron, A., et al. 2024, A&A, 682, L2

Birrer, S. & Amara, A. 2018, Physics of the Dark Universe, 22, 189

Birrer, S., Amara, A., & Refregier, A. 2017, J. Cosmology Astropart. Phys., 2017, 037

Birrer, S., Shajib, A., Gilman, D., et al. 2021, The Journal of Open Source Software, 6, 3283

Blondel, M., Berthet, Q., Cuturi, M., et al. 2021, arXiv preprint arXiv:2105.15183

Bocquet, S., Grandis, S., Bleem, L. E., et al. 2024, arXiv e-prints, arXiv:2401.02075

Bolton, A. S., Burles, S., Koopmans, L. V. E., Treu, T., & Moustakas, L. A. 2006, ApJ, 638, 703

Bozza, V., Pietroni, S., & Melchiorre, C. 2020, Universe, 6, 106

Bradač, M., Clowe, D., Gonzalez, A. H., et al. 2006, ApJ, 652, 937

Bradbury, J., Frostig, R., Hawkins, P., et al. 2018, JAX: composable transformations of Python+NumPy programs

Bulbul, E., Liu, A., Kluge, M., et al. 2024, arXiv e-prints, arXiv:2402.08452

Caminha, G. B., Grillo, C., Rosati, P., et al. 2023, A&A, 678, A3

Caminha, G. B., Suyu, S. H., Grillo, C., & Rosati, P. 2022, A&A, 657, A83

Cao, X., Li, R., Nightingale, J. W., et al. 2022, Research in Astronomy and Astrophysics, 22, 025014

Cappellari, M. 2017, MNRAS, 466, 798

Cappellari, M. & Emsellem, E. 2004, PASP, 116, 138

Cathey, J., Gonzalez, A. H., Lower, S., et al. 2023, arXiv e-prints, arXiv:2307.10115

Cava, A., Schaerer, D., Richard, J., et al. 2018, Nature Astronomy, 2, 76

Cheng, C., Huang, J.-S., Smail, I., et al. 2023, ApJ, 942, L19

Chirivì, G., Yıldırım, A., Suyu, S. H., & Halkola, A. 2020, A&A, 643, A135

Coe, D., Salmon, B., Bradač, M., et al. 2019, ApJ, 884, 85

Collett, T. E., Buckley-Geer, E., Lin, H., et al. 2017, ApJ, 843, 148

Dai, L., Kaurov, A. A., Sharon, K., et al. 2020, MNRAS, 495, 3192

Diego, J. M., Meena, A. K., Adams, N. J., et al. 2023, A&A, 672, A3

Diego, J. M., Molnar, S. M., Cerny, C., et al. 2020, ApJ, 904, 106

Ding, X., Silverman, J. D., & Onoue, M. 2022, ApJ, 939, L28

Du, W., Zhao, G.-B., Fan, Z., et al. 2020, ApJ, 892, 62

Dubinski, J. 1994, ApJ, 431, 617

Dubois, Y., Gavazzi, R., Peirani, S., & Silk, J. 2013, MNRAS, 433, 3297

Dutton, A. A. & Treu, T. 2014, MNRAS, 438, 3594

Edenhofer, G., Frank, P., Roth, J., et al. 2024, Re-Envisioning Numerical Information Field Theory (NIFTy.re): A Library for Gaussian Processes and Variational Inference

Edenhofer, G., Zucker, C., Frank, P., et al. 2023, arXiv e-prints, arXiv:2308.01295

Elíasdóttir, Á., Limousin, M., Richard, J., et al. 2007, arXiv e-prints, arXiv:0710.5636

Enßlin, T. A. 2019, Annalen der Physik, 531, 1800127

Etherington, A., Nightingale, J. W., Massey, R., et al. 2022, MNRAS, 517, 3275

Etherington, A., Nightingale, J. W., Massey, R., et al. 2023a, MNRAS, 521, 6005

Etherington, A., Nightingale, J. W., Massey, R., et al. 2023b, arXiv e-prints, arXiv:2301.05244

Euclid Collaboration, Adam, R., Vannier, M., et al. 2019, A&A, 627, A23

Frank, P., Leike, R., & Enßlin, T. A. 2021, Entropy, 23, 853

Frye, B. L., Pascale, M., Foo, N., et al. 2023, ApJ, 952, 81

Frye, B. L., Pascale, M., Pierel, J., et al. 2024, ApJ, 961, 171

Gaia Collaboration, Vallenari, A., Brown, A. G. A., et al. 2023, A&A, 674, A1

Galan, A., de Vyvere, L. V., Gomer, M. R., Vernardos, G., & Sluse, D. 2023, Journal of Open Source Software, 8, 5567

Galan, A., Peel, A., Joseph, R., Courbin, F., & Starck, J. L. 2021, A&A, 647, A176

Galan, A., Vernardos, G., Peel, A., Courbin, F., & Starck, J. L. 2022, A&A, 668, A155

Garvin, E. O., Kruk, S., Cornen, C., et al. 2022, A&A, 667, A141

Gavazzi, R., Fort, B., Mellier, Y., Pelló, R., & Dantel-Fort, M. 2003, A&A, 403, 11

Gavazzi, R., Treu, T., Marshall, P. J., Brault, F., & Ruff, A. 2012, ApJ, 761, 170

Gnedin, O. Y., Kravtsov, A. V., Klypin, A. A., & Nagai, D. 2004, ApJ, 616, 16

Gomer, M. & Williams, L. L. R. 2020, J. Cosmology Astropart. Phys., 2020, 045

Gomer, M. R., Ertl, S., Biggio, L., et al. 2023, A&A, 679, A59

Granata, G., Bergamini, P., Grillo, C., et al. 2023, A&A, 679, A124

Grillo, C., Karman, W., Suyu, S. H., et al. 2016, ApJ, 822, 78

Grillo, C., Pagano, L., Rosati, P., & Suyu, S. H. 2024, arXiv e-prints, arXiv:2401.10980

Grillo, C., Rosati, P., Suyu, S. H., et al. 2020, ApJ, 898, 87

Gu, A., Huang, X., Sheu, W., et al. 2022, ApJ, 935, 49

Hilton, M., Sifón, C., Naess, S., et al. 2021, ApJS, 253, 3

Hunter, J. D. 2007, Computing in Science & Engineering, 9, 90

Hutschenreuter, S., Haverkorn, M., Frank, P., Raycheva, N. C., & Enßlin, T. A. 2023, arXiv e-prints, arXiv:2304.12350

Jaelani, A. T., More, A., Oguri, M., et al. 2020, MNRAS, 495, 1291

Johansson, P. H., Naab, T., & Ostriker, J. P. 2012, ApJ, 754, 115

Jullo, E. & Kneib, J. P. 2009, MNRAS, 395, 1319

Kamieneski, P. S., Frye, B. L., Pascale, M., et al. 2023, ApJ, 955, 91

Karchev, K., Coogan, A., & Weniger, C. 2022, MNRAS[arXiv:2105.09465]

Keel, W. C., Windhorst, R. A., Jansen, R. A., et al. 2023, AJ, 165, 166

Kelly, P. L., Rodney, S., Treu, T., et al. 2023, Science, 380, abh1322

Klein, M., Hernández-Lang, D., Mohr, J. J., Bocquet, S., & Singh, A. 2023, MNRAS, 526, 3757

Kluyver, T., Ragan-Kelley, B., Pérez, F., et al. 2016, in Positioning and Power in Academic Publishing: Players, Agents and Agendas, ed. F. Loizides & B. Schmidt, IOS Press, 87 – 90

Knollmüller, J. & Enßlin, T. A. 2019, arXiv e-prints, arXiv:1901.11033

Kochanek, C. S. 2020, MNRAS, 493, 1725

Lewis, A. 2019, arXiv e-prints, arXiv:1910.13970

Marriage, T. A., Acquaviva, V., Ade, P. A. R., et al. 2011, ApJ, 737, 61

Menanteau, F., Hughes, J. P., Sifón, C., et al. 2012, ApJ, 748, 7

Meneghetti, M., Cui, W., Rasia, E., et al. 2023, A&A, 678, L2

Meneghetti, M., Ragagnin, A., Borgani, S., et al. 2022, A&A, 668, A188

Michalewicz, K., Millon, M., Dux, F., & Courbin, F. 2023, The Journal of Open Source Software, 8, 5340

Millon, M., Galan, A., Courbin, F., et al. 2020, A&A, 639, A101

Millon, M., Michalewicz, K., Dux, F., Courbin, F., & Marshall, P. J. 2024, arXiv e-prints, arXiv:2402.08725

Monna, A., Seitz, S., Zitrin, A., et al. 2015, MNRAS, 447, 1224

Mozumdar, P., Fassnacht, C. D., Treu, T., Spiniello, C., & Shajib, A. J. 2023, A&A, 672, A20

Natarajan, P., Kneib, J.-P., & Smail, I. 2002, ApJ, 580, L11

Natarajan, P., Williams, L. L. R., Bradač, M., et al. 2024, Space Sci. Rev., 220, 19

Newman, A. B., Treu, T., Ellis, R. S., & Sand, D. J. 2011, ApJ, 728, L39

Newman, A. B., Treu, T., Ellis, R. S., & Sand, D. J. 2013, ApJ, 765, 25

Nocedal, J. & Wright, S. J. 2006, Numerical Optimization, 2nd edn., Springer Series in Operations Research and Financial Engineering (New York: Springer)

Oliphant, T. E. 2006, A guide to NumPy, Vol. 1 (Trelgol Publishing USA)

Orban de Xivry, G. & Marshall, P. 2009, MNRAS, 399, 2

Planck Collaboration, Ade, P. A. R., Aghanim, N., et al. 2016, A&A, 594, A27

Powell, D. M., Vegetti, S., McKean, J. P., et al. 2022, MNRAS, 516, 1808

Price-Whelan, A. M., Sipőcz, B. M., Günther, H. M., et al. 2018, AJ, 156, 123

Rigby, J. R., Vieira, J. D., Phadke, K. A., et al. 2023, arXiv e-prints, arXiv:2312.10465

Rizzo, F., Vegetti, S., Fraternali, F., & Di Teodoro, E. 2018, MNRAS, 481, 5606

Rodney, S. A., Brammer, G. B., Pierel, J. D. R., et al. 2021, Nature Astronomy, 5, 1118

Rüstig, J., Guardiani, M., Roth, J., Frank, P., & Enßlin, T. 2024, A&A, 682, A146

Rusu, C. E., Wong, K. C., Bonvin, V., et al. 2020, MNRAS, 498, 1440

Sánchez-Blázquez, P., Peletier, R. F., Jiménez-Vicente, J., et al. 2006, MNRAS, 371, 703

Schaye, J., Crain, R. A., Bower, R. G., et al. 2015, MNRAS, 446, 521

Schneider, P. 1985, A&A, 143, 413

Schneider, P. & Sluse, D. 2013, A&A, 559, A37

Schneider, P. & Weiss, A. 1986, A&A, 164, 237

Schuldt, S., Chirivì, G., Suyu, S. H., et al. 2019, A&A, 631, A40

Selig, M., Bell, M. R., Junklewitz, H., et al. 2013, Astronomy Astrophysics, 554, A26

Sérsic, J. L. 1963, Boletin de la Asociacion Argentina de Astronomia La Plata Argentina, 6, 41

Shajib, A. J., Birrer, S., Treu, T., et al. 2020, MNRAS, 494, 6072

Shajib, A. J., Mozumdar, P., Chen, G. C. F., et al. 2023, A&A, 673, A9

Shajib, A. J., Treu, T., Birrer, S., & Sonnenfeld, A. 2021, MNRAS, 503, 2380

Shin, E. M. & Evans, N. W. 2008, MNRAS, 390, 505

Shu, Y., Bolton, A. S., Kochanek, C. S., et al. 2016, ApJ, 824, 86

Sluse, D., Chantry, V., Magain, P., Courbin, F., & Meylan, G. 2012, A&A, 538, A99

Sonnenfeld, A. 2018, MNRAS, 474, 4648

Sonnenfeld, A., Treu, T., Gavazzi, R., et al. 2013, ApJ, 777, 98

Steininger, T., Dixit, J., Frank, P., et al. 2019, Annalen der Physik, 531, 1800290

Stone, M. A., Lyu, J., Rieke, G. H., & Alberts, S. 2023, ApJ, 953, 180

Suyu, S. H. & Halkola, A. 2010, A&A, 524, A94

Suyu, S. H., Hensel, S. W., McKean, J. P., et al. 2012, ApJ, 750, 10

Suyu, S. H., Treu, T., Hilbert, S., et al. 2014, ApJ, 788, L35

Tamura, Y., Oguri, M., Iono, D., et al. 2015, PASJ, 67, 72

Tan, C. Y., Shajib, A. J., Birrer, S., et al. 2023, arXiv e-prints, arXiv:2311.09307

Tessore, N. & Metcalf, R. B. 2015, A&A, 580, A79

Tremmel, M., Karcher, M., Governato, F., et al. 2017, MNRAS, 470, 1121

Treu, T., Koopmans, L. V., Bolton, A. S., Burles, S., & Moustakas, L. A. 2006, ApJ, 640, 662

Treu, T. & Koopmans, L. V. E. 2002, MNRAS, 337, L6

Umetsu, K., Sereno, M., Tam, S.-I., et al. 2018, ApJ, 860, 104

Valdes, F., Gupta, R., Rose, J. A., Singh, H. P., & Bell, D. J. 2004, ApJS, 152, 251

Van de Vyvere, L., Sluse, D., Gomer, M. R., & Mukherjee, S. 2022, A&A, 663, A179

Van Der Walt, S., Colbert, S. C., & Varoquaux, G. 2011, Computing in Science & Engineering, 13, 22

Vegetti, S., Czoske, O., & Koopmans, L. V. E. 2010, MNRAS, 407, 225

Virtanen, P., Gommers, R., Oliphant, T. E., et al. 2020, Nature Methods, 17, 261

Wang, B., Fujimoto, S., Labbé, I., et al. 2023, ApJ, 957, L34

Wang, B., Leja, J., Labbé, I., et al. 2024, ApJS, 270, 12

Wang, H., Cañameras, R., Caminha, G. B., et al. 2022, A&A, 668, A162

Welch, B., Coe, D., Diego, J. M., et al. 2022, Nature, 603, 815

Wen, Z. L., Han, J. L., & Liu, F. S. 2012, ApJS, 199, 34

Williams, L. L. R., Kelly, P. L., Treu, T., et al. 2024, ApJ, 961, 200

Windhorst, R. A., Cohen, S. H., Jansen, R. A., et al. 2023, AJ, 165, 13

Wong, K. C., Suyu, S. H., & Matsushita, S. 2015, ApJ, 811, 115

Zitrin, A., Menanteau, F., Hughes, J. P., et al. 2013, ApJ, 770, L15

Appendix A: Complementary results and discussion

Appendix A.1: Surface brightness properties of the deflectors

We show in Fig. A.1 the best-fit models for the deflectors surface brightness, and measurements of effective radius and aperture magnitudes are indicated in Table A.1. We obtain a first-order approximation of model parameters uncertainties using the Fisher information matrix, by inverting the Hessian matrix of the loss function evaluated at the best-fit position. However, depending on the application, we caution on using these uncertainties for galaxies L1 and L2, as their surface brightness is significantly more complex than the smooth light profiles we used.

Appendix A.2: Full joint posterior distribution of mass model parameters

In Sect. 5.3 we present constraints on mass model parameters given the three model families that we assumed. For completeness, we show in Fig. A.2 the full version of Fig. 9, that shows the entire set of mass model parameters that are inferred (jointly with the source model). Since our lens surface brightness informs motivated priors for the centroids, axis ratio and position angle of the EPL profiles, we also indicate with dashed lines the best-fit values from our light models for L1 and L2. This completes Fig. 10, which illustrates the offset between the centroid of the lens and mass distributions of these elliptical galaxies.

Appendix A.3: Robustness of the constraints

As detailed in Sect. 4.3, we already include in the marginalized posterior distributions of Fig. 9 several of model variations within a given model family, including changing the initial parameters values. Here we investigate further the robustness of our inference and look for possible systematic errors due to specific modeling choices.

We vary the overall source grid resolution, namely in the number of pixels along each spatial dimension. As mentioned in Sect. 4.6, we selected the fiducial number of source pixels $n_{src} = 100$ from a series of preliminary models, and noticed that the χ^2_ν value does not significantly vary when increasing n_{src}. Nevertheless, drastically increasing the source resolution (e.g., doubling or tripling it) can still provide a slightly better fit to the data—essentially capturing unresolved point-like features in the arc. However, given the much larger number of parameters (due to the multi-band field model parametrization), these models are heavily disfavored by the BIC. Here we show the inference results after setting $n_{src} = 300$, namely tripling our fiducial source resolution. The resulting posteriors are shown as dotted lines in Fig. A.3 for a subset of mass model parameters.

We also investigate whether the choice of variational inference algorithm impact the estimation of the posterior distribution. Given the large number of parameters, it may be expected to have different algorithms converging to difference locations in parameter space, potentially providing different uncertainty estimations. We do so by replacing the sampler type `'geometric'` (GEOVI) by `'altmetric'` within NIFTY. The main difference between `'geometric'` and `'altmetric'` methods reside in the resampling step performed at each iteration. The resulting posteriors are indicated in Fig. A.3 with dashed lines.

Finally, we investigate the impact of the uncertainty on the cluster-scale mass distribution. We randomly draw 20 posterior samples from the cluster model of Caminha et al. (2023) and run our inference pipeline using each the corresponding deflection field samples (with identical initial position in the parameter space). The resulting posteriors, marginalized over the 20 cluster deflection field posterior samples, is indicated in Fig. A.3 with dotted-dashed lines. We note that among these cluster-scale posterior samples, some are leading to sensibly better fit to the imaging data, compared to the best-fit model we use throughout this work. Therefore, *El Anzuelo* strong lensing features seem to provide extra constraints also on the large scale component (i.e., the cluster-scale dark matter halo) of the cluster.

From all the additional models we run, we find that all posterior distributions remain statistically compatible with those of our fiducial model. Therefore, we conclude that, among the many modeling choices we have explored, we do not find a significant source of systematic error in our lens model of *El Anzuelo*.

Appendix A.4: Fifth and central images in strong lenses

As shown in Sect. 5.4, we confirm the five-image lensing configuration of *El Anzuelo*. This is a rather rare situation: in only a few galaxy-scale strong lenses with a single or two main deflectors has been discovered a fifth extended, non-demagnified image. The vast majority of fifth images fall in the category of unresolved demagnified central images, which appear close to the deflector centroid and are often only detected at radio wavelengths thanks to weaker contamination from the lens light (e.g., Gavazzi et al. 2003; Tamura et al. 2015; Wong et al. 2015; Collett et al. 2017). The appearance of extended source features in the vicinity of L1 and L3 centroids may provide constraints on the inner part of the mass density profile of the deflectors (at the cost of larger blending between the light of the various components). A comparable configuration in the literature is the Cosmic Horseshoe strong lens, for which Schuldt et al. (2019) used the image of a second lensed source appearing close to the lens galaxy to constrain the inner dark matter profile of that galaxy. However, as it is the case for the Cosmic Horseshoe, the fifth image often corresponds to a *radial image* (as opposed to much more common *tangential images*). Coming back to *El Anzuelo*, the fifth of the source remains a tangential one, thus making it a very peculiar lensing configuration. Although not entirely comparable, strong lens systems in which a low-mass satellite galaxy coincides with a strongly lensed arc and locally creates additional strong lensing features can give rise to additional tangential images (see systems analysed in Suyu & Halkola 2010; Vegetti et al. 2010).

Appendix B: Spectral energy distribution of a source clump

We show in Fig. B.1 the spectral energy distribution (SED) of one of the point-like features in the western part of the arc (image 2b in Fig. 11). We subtract the lens light, the arc light and integrate the observed flux within a circular aperture with radius $0\farcs2$. Since our source model does not capture extremely compact (likely unresolved) features like image 2b and other counter-images, it can be subtracted from the data to perform reasonably good aperture photometry.

Table A.1. Summary of photometric properties measured from the JWST data.

Deflector	L1		L2		L3	
JWST filter	θ_{eff} [″]	m_{AB} [mag]	θ_{eff} [″]	m_{AB} [mag]	θ_{eff} [″]	m_{AB} [mag]
F150W	0.57 ± 0.02	18.95 ± 0.05	0.39 ± 0.03	20.68 ± 0.05	0.16 ± 0.02	20.47 ± 0.05
F200W	0.61 ± 0.01	18.53 ± 0.05	0.36 ± 0.02	20.25 ± 0.05	0.15 ± 0.01	20.07 ± 0.05
F277W	0.62 ± 0.01	18.32 ± 0.05	0.30 ± 0.02	20.18 ± 0.05	0.16 ± 0.01	19.780 ± 0.05
F356W	0.54 ± 0.01	18.32 ± 0.05	0.29 ± 0.01	20.10 ± 0.05	0.15 ± 0.02	19.81 ± 0.05
F410M	0.54 ± 0.01	18.45 ± 0.05	0.26 ± 0.01	20.13 ± 0.05	0.15 ± 0.01	19.10 ± 0.05
F444W	0.60 ± 0.01	18.63 ± 0.05	0.30 ± 0.01	20.25 ± 0.05	0.15 ± 0.01	20.17 ± 0.05

Notes. Quoted uncertainties only include statistical errors, hence are likely underestimated given the quality of fit to the imaging data. Uncertainties on the reported AB magnitudes have been artificially inflated to a more conservative 50 mmag.
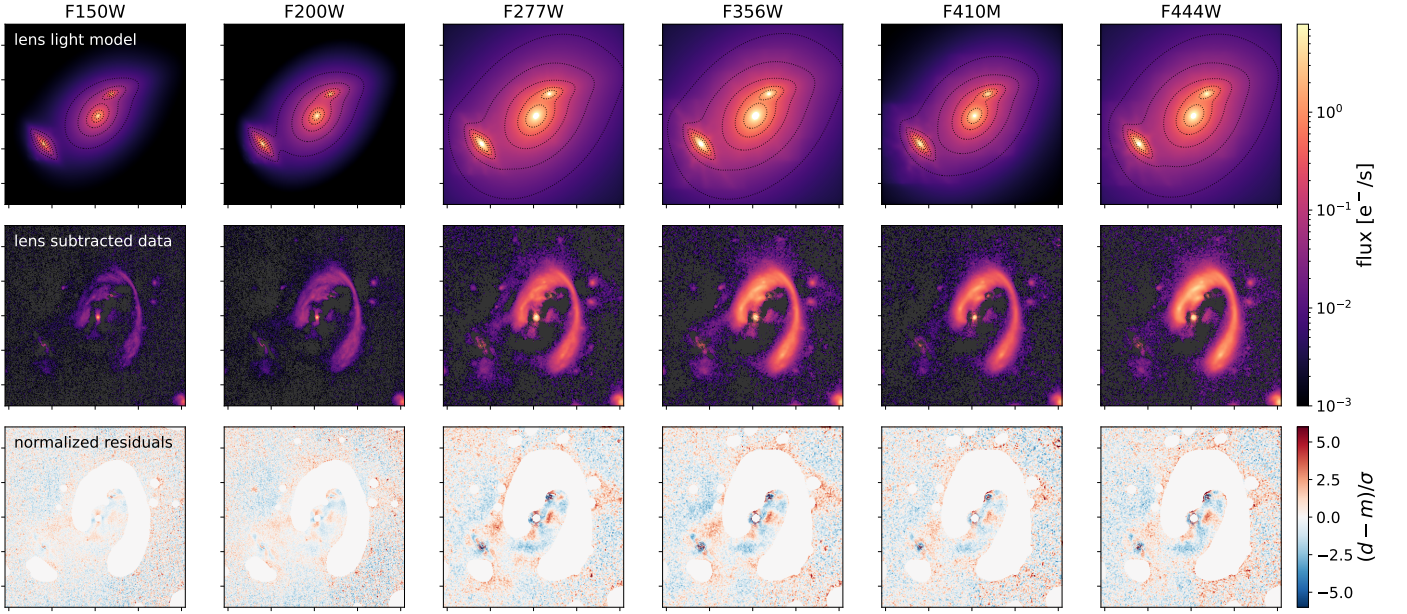

Fig. A.1. Best-fit models of the deflectors surface brightness of *El Anzuelo*, for each of the six JWST filters considered in this work. *First row:* model of the surface brightness of L1, L2 (two concentric Sérsic profiles) and L3 deflectors (three concentric profiles). *Middle row:* data after subtraction of the best-fit model shown in first row. Negative pixels are displayed in dark gray in these panels. *Bottom row:* normalized residuals maps corresponding to the best-fit models. White areas indicate pixels that were masked out (lensed arcs and nearby non-modeled objects) during the fit of the lens light distribution.
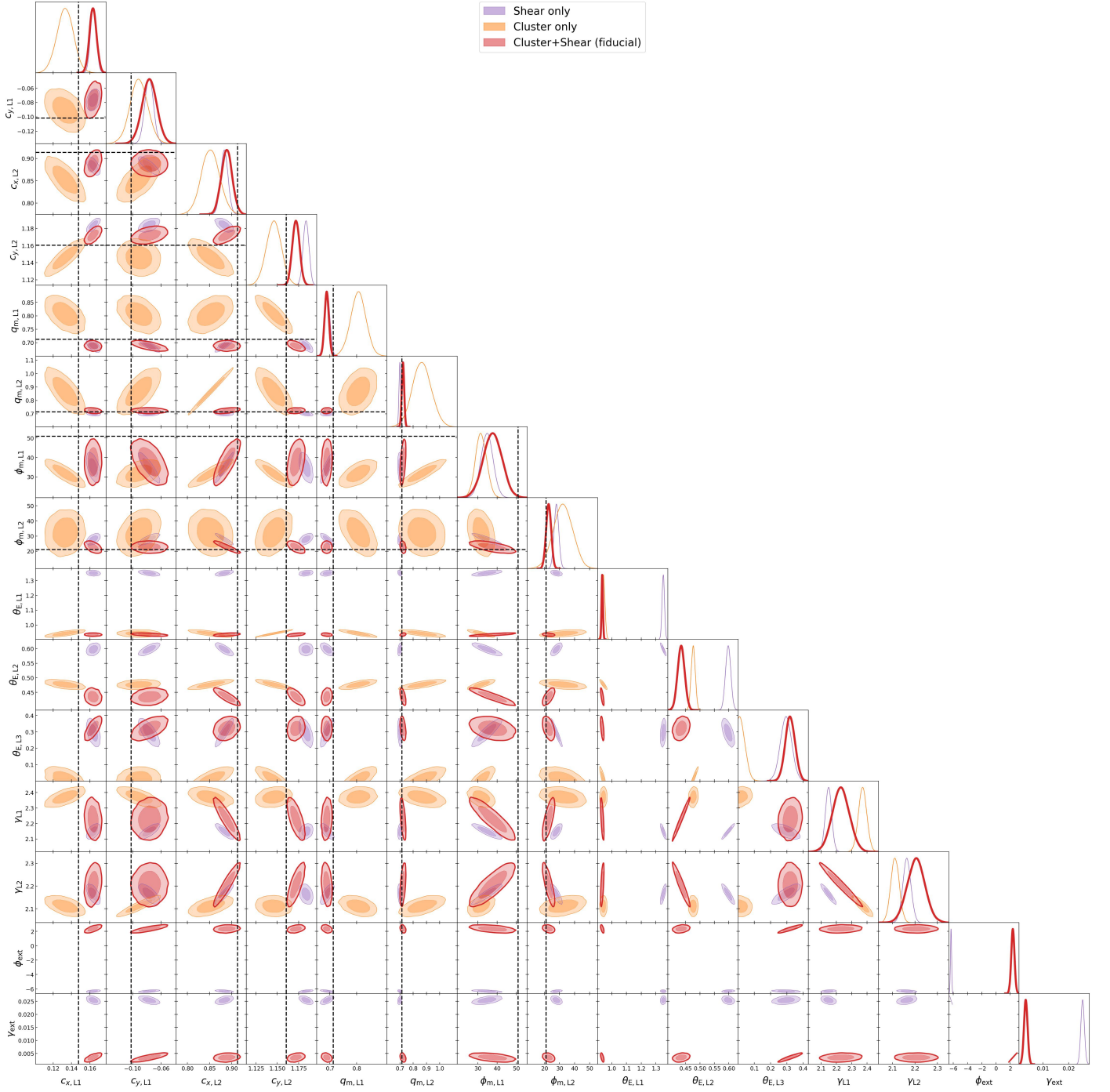
Fig. A.2. Full version of Fig. 9, showing the joint posterior distribution of a subset of lens mass parameters, for the 3 main model families tested in this work. The first one includes only external shear in addition of the three main deflectors, the second one replaces external shear with the *El Gordo* cluster deflection field, and the last one includes a combination of the two. Dashed lines indicate the mean position (over the six filters), position angles and axis ratios of the deflectors light, to compare with the values inferred from lensing.
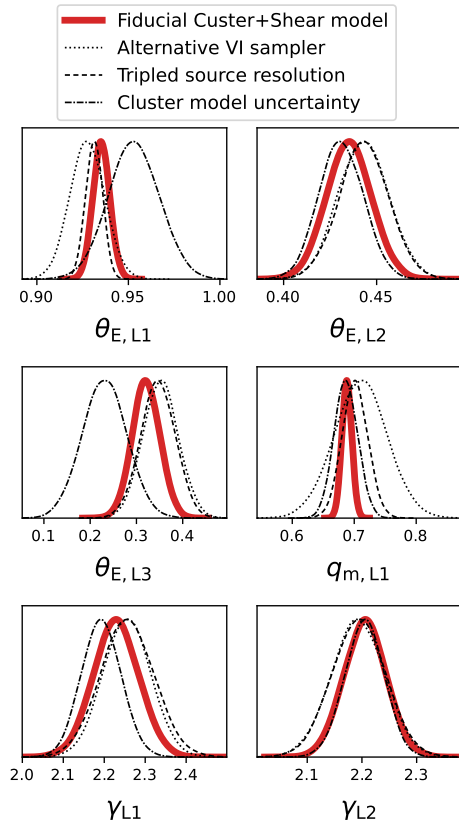
Fig. A.3. Systematic checks to test the robustness of the model. Three additional posterior distributions are shown, associated to different modeling and sampling choices.
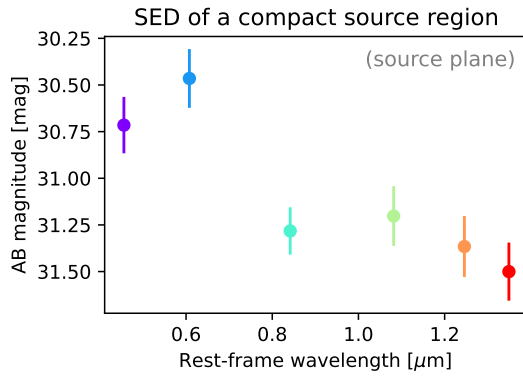

Fig. B.1. Spectral energy distribution of image 2b shown in the top right panel of Fig. 11, from the six JWST/NIRCam filters considered in this work. The x axis shows rest-frame wavelength assuming a source red-shift of $z_{\mathrm{s}} = 2.291$ and the y axis shows de-magnified AB magnitudes, integrated within a circular aperture of radius $0\rlap{.}{''}2$, after subtraction of both the lens and source light models.